514

HELIOS A
MICROMETERIOD IMPACT DATA
74-097A-12A ,12B

514	74-097A-12A	SPIS-00001	HELIOS 1
514	74-097A-12B	PSSB-00045	HELIOS 1

Table of Contents

1. Introduction
2. Errata/Change Log
3. LINKS TO RELEVANT INFORMATION IN THE ONLINE NSSDC INFORMATION SYSTEM
4. Catalog Materials
    a. Associated Documents
    b. Core Catalog Materials

---

1. INTRODUCTION:

The documentation for this data set was originally on paper, kept in NSSDC's Data Set Catalogs (DSCs). The paper documentation in the Data Set Catalogs have been made into digital images, and then collected into a single PDF file for each Data Set Catalog. The inventory information in these DSCs is current as of July 1, 2004. This inventory information is now no longer maintained in the DSCs, but is now managed in the inventory part of the NSSDC information system. The information existing in the DSCs is now not needed for locating the data files, but we did not remove that inventory information.

The offline tape datasets have now been migrated from the original magnetic tape to Archival Information Packages (AIP's).

A prior restoration may have been done on data sets, if a requestor of this data set has questions; they should send an inquiry to the request office to see if additional information exists.

2. ERRATA/CHANGE LOG:

NOTE: Changes are made in a text box, and will show up that way when displayed on screen with a PDF reader.

When printing, special settings may be required to make the text box appear on the printed output.

Version	Date	Person	Page	Description of Change
01				
02				

3 LINKS TO RELEVANT INFORMATION IN THE ONLINE NSSDC INFORMATION SYSTEM:

http://nssdc.gsfc.nasa.gov/nmc/

[NOTE: This link will take you to the main page of the NSSDC Master Catalog. There you will be able to perform searches to find additional information]

4. CATALOG MATERIALS:

a. Associated Documents — To find associated documents you will need to know the document ID number and then click here.
http://nssdcftp.gsfc.nasa.gov/miscellaneous/documents/

b. Core Catalog Materials

HELIOS-A

MICROMETEOROID IMPACT DATA

74-097A-12A SPIS-00001

This data set has been restored. There was originally one 9-track, 1600 BPI tape written in Binary. There is one restored tape. The DR tape is a 3480 cartridge and the DS tape is 9-track, 6250 BPI. The original tape was created on a DEC10 computer and the restored tape was created on an IBM 9021 computer. The DR and DS numbers along with the corresponding D number are as follows:

DR#	DS#	D#	FILES	TIME SPAN
DR005294	DS005294	D046013	1	12/19/74 - 01/02/80

HELIOS-A

MICROMETEOROID IMPACT DATA

74-097A-12A, 12B

This data set has been restored. There was originally one 9-track, 1600 BPI tape written in Binary. There is one restored tape. The DR tape is a 3480 cartridge and the DS tape is 9-track, 6250 BPI. The original tape was created on a DEC10 computer and the restored tape was created on an IBM 9021 computer. The DR and DS numbers along with the corresponding D number are as follows:

DR#	DS#	D#	FILES	TIME SPAN	
DR005294	DS005294	D046013	1	12/19/74 - 01/02/80	12A
		"	2	"	12B

** 2nd file have an ASCII listing of 1st file.

REQ. AGENT	RAND NO.	ACQ. AGENT
DEW	V0106	HKH

HELIOS A
MICROMETEORIOD IMPACT DATA
74-097A-12A

This data set consists of 1 magnetic tape. The tape is 1600 BPI, 9 track, binary with one file of data on it. The tape was created on a DEC-10 computer.

D#	C#	TIME SPAN
D-46103	C-21794	12/19/74 - 01/02/80

This is the format for the ASCII version of the Micrometeoroid data.

```
C *** THE DATA ARE CONTAINED IN ONE FILE, SO THE PROGRAM  ***
C *** WRITES THE OUTPUT TO A DISK FILE.  THERE ARE 203    ***
C *** ACTIVE TIME RECORDS CONTAINING 4 REAL WORDS EACH,   ***
C *** FOLLOWED BY 235 PARTICLE DATA RECORDS CONTAINING 47 ***
C *** REAL WORDS EACH.  ALL WORDS ARE FORMATTED AS E10.4  ***
```

MAX-PLANCK-INSTITUT FÜR KERNPHYSIK

D-6900 HEIDELBERG 1
Postfach 103980
Saupfercheckweg 1 (beim Bierhelder Hof)
Telefon Sammel-Nr. (06221) 5161
Durchwahl (06221) 516
Telex 461666

July 30, 1981

James I. Vette
World Data Center A
Rockets and Satellites
Goddard Space Flight Center Code 601
Greenbelt, Maryland
20771 U.S.A.

Dear Mr. Vette,

In response to your letter of the 4th of June 1981 to Dr. Fechtig, I should like to send you a data-tape with the active times and the scientific results (micrometeoroid impact data) of our HELIOS A experiment E 10 together with the description.

Yours sincerely
W. Inka Rimpler
W. Inka Rimpler

MAX-PLANCK-INSTITUT FÜR KERNPHYSIK
HEIDELBERG

DESCRIPTION OF THE DATA
OF THE
HELIOS A MICROMETEOROID EXPERIMENT
E 10

MAX-PLANCK-INSTITUT FÜR KERNPHYSIK
SAUPFERCHECKWEG 1
D-6900 HEIDELBERG
FEDERAL REPUBLIC OF GERMANY

JULY 1981

AUTHOR: W. INKA RIMPLER

Table of contents

1. General information to the data tape

2. Program that produced the data tape

3. Description of the Number System of the DEC-10

4. Description of the Tape Format

5. Description of the structure of the data on the tape

General Information to the data tape

The data are written on a 9 track tape with 1600 BPI, using a FORTRAN-program. The records are written on the tape in a binary DEC-10-style. The data ends with an EOF-mark.

The added program shows how the tape was written.
As well we added a copy of the Hardware Reference Manual, describing the Number System and the Tape Format of the DEC-10. The organisation of the data and the scientific meaning of every word you will find in the added description.

```
*
*
*       PROGRAM WRITES HELIOS A DATA FROM DISK ON TAPE
*       MOUNT MTA:3/REELID:D7XX01/V:"1600 BPI,9 TRACK"/WRITE:YES
*       EXE WDS.FOR,IUTIL.REL
*
*       AUTHOR:         W.I.RIMPLER
*       DATE:           15-07-81
*       MACHINE:        DEC-10
*       LANGUAGE:       FORTRAN IV
*
*
*
*
*
*
*
        REAL*8 MOUT(48),RR,RL,ZSI(66),C(250)
        DIMENSION XMZ(4), IREC(2219), ISDB(500), SDAT(47),
     &  CH(12)
       REAL*8 DLSSP,RNDLSS,FULTIM,RAZA,DELRH,DELRAS,WTIME,QSP
       INTEGER IA,IT,EA,ET,PF,PE,SEC,AD,AA,PC,SC,LC,DC,TP,WI,DI,O1,O2,E
     FSI,MI,TI,BR,FM,ECT,SCD,SCH,SCM,SCMS,SPECTR(45),TIDE,GMD,GMH,GMM,
     FGMMS,O1O2C,EDSIC,IAMI,BCT,SSP,TSPC,DATEC,ESA,FOURY(45),ECTCK,
     FISPEIC,KENNUN,IENDBL
       EQUIVALENCE(DLSSP,ISDB(347)),(RNDLSS,ISDB(400))
       EQUIVALENCE(ISDB(323),FULTIM),(ISDB(327),BLOCKE)
     F,(ISDB(351),RAZA)
     F,(ISDB(332),DELRH)
     F,(ISDB(334),DELRAS)
     F,(ISDB(336),WTIME)
     F,(ISDB(3),FM)
     F,(ISDB(4),BR)
     F,(ISDB(7),IDM)
     F,(ISDB(9),GMD)
     F,(ISDB(10),GMH)
     F,(ISDB(11),GMM)
       EQUIVALENCE(ISDB(12),GMMS)
     F,(ISDB(13),SCD)
     F,(ISDB(14),SCH)
     F,(ISDB(15),SCM)
     F,(ISDB(16),SCMS)
     F,(ISDB(19),IA)
     F,(ISDB(20),IT)
     F,(ISDB(21),EA)
     F,(ISDB(22),ET)
     F,(ISDB(23),PF)
     F,(ISDB(24),PE)
       EQUIVALENCE (ISDB(25),ECT)
     F,(ISDB(26),TIDE)
     F,(ISDB(27),TI)
     F,(ISDB(28),SEC)
     F,(ISDB(29),AD)
     F,(ISDB(31),AA)
     F,(ISDB(32),PC)
     F,(ISDB(33),SC)
     F,(ISDB(34),LC)
     F,(ISDB(35),DC)
     F,(ISDB(36),ED)
       EQUIVALENCE(ISDB(37),SI)
```

```
    F,(ISDB(38),O1)
    F,(ISDB(39),O2)
    F,(ISDB(40),TP)
    F,(ISDB(41),WI)
    F,(ISDB(42),DI)
    F,(ISDB(43),MI)
    F,(ISDB(44),SPECTR)
    F,(ISDB(325),KENNUN)
    F,(ISDB(326),BCT)
    F,(ISDB(329),IENDBL)
     EQUIVALENCE(ISDB(338),ISPEIC)
    F,(ISDB(341),O102C)
    F,(ISDB(342),EDSIC)
    F,(ISDB(343),DATEC)
    F,(ISDB(344),IAMI)
    F,(ISDB(346),SSP)
    F,(ISDB(349),TSPC)
    F,(ISDB(350),ESA)
    F,(ISDB(353),FOURY)
    F,(ISDB(398),ECTCK)
      REAL*8 QCB,RVU,RV,RVO,RMU,RM,RMO
     EQUIVALENCE(ISDB(410),RV),(RM,ISDB(416))
    F,(ISDB(406),QCB),(ISDB(408),RVU),(ISDB(412),RVO),(ISDB(414),RMU)
    F,(ISDB(418),RMO),(ISDB(420),QSP)
*
*
      EQUIVALENCE(IREC(83),RR),(IREC(81),RL),(ZSI,IREC(585)),
    & (IREC(1219),C)
*
*
*
      OPEN(UNIT=1,DEVICE='DSK',ACCESS='SEQIN',MODE='BINARY',
    & RECORDSIZE=96,FILE='MZHIG.OUT')
      OPEN(UNIT=2,DEVICE='DSK',ACCESS='SEQIN',MODE='BINARY',
    & RECORDSIZE=2219,FILE='ALL.DAT')
      OPEN(UNIT=3,DEVICE='MTA',DENSITY='1600',MODE='BINARY',
    & ACCESS='SEQOUT')
*
*
*
      REWIND 3
*
*
*     ACTIVE TIME ON TAPE
*
*
      DO 26 IK=1,4
 26   READ(1) MOUT
      DO 1 I=1,202
      DO 3 K=1,4
      XMZ(K)=0.
 3    CONTINUE
      DO 2 J=1,10
      READ(1,END=666,ERR=777) MOUT
      XMZ(1)=XMZ(1)+MOUT(17)
      XMZ(2)=XMZ(2)+MOUT(29)
      XMZ(3)=XMZ(3)+(MOUT(22)+MOUT(23)+MOUT(24))/3.
      XMZ(4)=XMZ(4)+(MOUT(30)+MOUT(31)+MOUT(32))/3.
 2    CONTINUE
      DO 4 K=1,4
```

```
      XMZ(K)=XMZ(K)/864000.
    4 CONTINUE
      WRITE(3,END=888,ERR=999) XMZ
    1 CONTINUE
      DO 5 K=1,4
      XMZ(K)=0.
    5 CONTINUE
      DO 6 K=1,4
      READ(1,END=666,ERR=777) MOUT
      XMZ(1)=XMZ(1)+MOUT(17)
      XMZ(2)=XMZ(2)+MOUT(29)
      XMZ(3)=XMZ(3)+(MOUT(22)+MOUT(23)+MOUT(24))/3.
      XMZ(4)=XMZ(4)+(MOUT(30)+MOUT(31)+MOUT(32))/3.
    6 CONTINUE
      DO 7 K=1,4
      XMZ(K)=XMZ(K)/4.
      XMZ(K)=XMZ(K)/86400.
    7 CONTINUE
      WRITE(3,END=888,ERR=999) XMZ
*
*
*     PARTICLES ON TAPE
*
      DO 8 I=1,235
      READ(2,END=666,ERR=777) IREC
      DO 9 J=1,500
    9 ISDB(J)=IREC(J+84)
      SDAT(1)=FLOAT(I)
      SDAT(2)=FLOAT(IREC(8))
      SDAT(3)=FLOAT(IREC(10))
      SDAT(4)=FLOAT(IREC(12))
      SDAT(5)=FLOAT(IREC(14))
      SDAT(6)=FLOAT(IREC(16))
      SDAT(7)=FLOAT(DI)
      SDAT(8)=RVU
      SDAT(9)=RV
      SDAT(10)=RVO
      SDAT(11)=RMU
      SDAT(12)=RM
      SDAT(13)=0.
      IF(IA.EQ.16.OR.EA.EQ.16) SDAT(13)=1.
      SDAT(14)=RMO
      SDAT(15)=RR
      SDAT(16)=RL
      APEX=WINKEL(ISDB(28),ISDB(42))
      SDAT(17)=APEX
      SDAT(18)=FLOAT(IREC(32))
      SDAT(19)=QSP
      SDAT(20)=4.
      IF(IA.LE.12) SDAT(20)=3
      IF(IA.LE.7) SDAT(20)=2
      IF(IA.LE.4) SDAT(20)=1
      SDAT(21)=FLOAT(LC)
      XHYP1=ZSI(1)+ZSI(2)
      XHYP2=ZSI(23)+ZSI(24)
      XHYP3=ZSI(45)+ZSI(46)
      IHYP=3
      IF(XHYP1.GE.0.75) IHYP=0
      IF(IHYP.EQ.0) GOTO 40
      IF(XHYP2.GE.0.75) IHYP=1
```

```
      IF(IHYP.EQ.1) GOTO 40
      IF(XHYP3.GE.0.75) IHYP=2
   40 CONTINUE
      IF(ZSI(25).EQ.9999.OR.XHYP2.GE.0.99) ZSI(25)=0.
      IF(ZSI(26).EQ.9999.OR.XHYP2.GE.0.99) ZSI(26)=0.
      IF(ZSI(29).EQ.9999.OR.XHYP2.GE.0.99) ZSI(29)=1.
      IF(ZSI(30).EQ.9999.OR.XHYP2.GE.0.99) ZSI(30)=1.
      ZSI(35)=ZSI(35)-0.02
      SDAT(22)=ZSI(25)
      SDAT(23)=ZSI(26)
      SDAT(24)=ZSI(29)
      SDAT(25)=ZSI(30)
      SDAT(26)=ZSI(31)
      SDAT(27)=ZSI(32)
      SDAT(28)=ZSI(35)
      SDAT(29)=ZSI(36)
      SDAT(30)=ZSI(23)+ZSI(27)
      SDAT(31)=ZSI(23)+ZSI(24)
      SDAT(32)=FLOAT(IHYP)
      SDAT(33)=0.
      IF(IREC(103).EQ.16) SDAT(33)=1.
      XD=0.
      XLD=RM*RV**2.2
      IF(XLD.GT.1.15E-10.AND.IREC(32).EQ.1.AND.IREC(126)
     & .EQ.1) XD=1.
      SDAT(34)=XD
      IF(IREC(2219).EQ.'U') XKENN=1.
      IF(IREC(2219).EQ.'C') XKENN=2.
      IF(IREC(2219).EQ.'E') XKENN=3.
      SDAT(35)=XKENN
      CMAX=0.
      DO 24 K=1,250
      IF(C(K).GE.CMAX)CMAX=C(K)
   24 CONTINUE
      CHSUM=0.
      DO 25 K=1,225
   25 CHSUM=CHSUM+C(K)
      IF(CHSUM.EQ.0.) CHSUM=1.
      CALL ISET(CH,12,0)
      DO 41 K=1,24
   41 CH(1)=CH(1)+C(K)/CHSUM
      DO 11 K=25,49
   11 CH(2)=CH(2)+C(K)/CHSUM
      DO 12 K=50,73
   12 CH(3)=CH(3)+C(K)/CHSUM
      DO 13 K=74,94
   13 CH(4)=CH(4)+C(K)/CHSUM
      DO 14 K=95,114
   14 CH(5)=CH(5)+C(K)/CHSUM
      DO 15 K=115,132
   15 CH(6)=CH(6)+C(K)/CHSUM
      DO 16 K=133,149
   16 CH(7)=CH(7)+C(K)/CHSUM
      DO 17 K=150,166
   17 CH(8)=CH(8)+C(K)/CHSUM
      DO 18 K=167,182
   18 CH(9)=CH(9)+C(K)/CHSUM
      DO 19 K=183,197
   19 CH(10)=CH(10)+C(K)/CHSUM
      DO 20 K=198,212
```

```
      DO 21 K=213,225
21    CH(12)=CH(12)+C(K)/CHSUM
      DO 10 J=1,12
      SDAT(J+35)=CH(J)
10    CONTINUE
      WRITE(3,END=888,ERR=999) SDAT
8     CONTINUE
      END FILE 3
      STOP
666   STOP' EOF BEI READ'
777   STOP' PARITY-ERROR IN READ'
999   STOP' PARITY-ERROR TAPE'
888   STOP' EOF IN WRITE'
      END
```

```
      FUNCTION WINKEL(JSEC,JDI)
      INTEGER JSEC,JDI
      IF(JDI.EQ.0)WINKEL=(JSEC-88.)*360./128.
      IF(JDI.EQ.1)WINKEL=(JSEC-56.)*360./128.
      IF(WINKEL.LT.0.)WINKEL=WINKEL+360.
      RETURN
      END
```

Number System

A program can interpret a data word as a 36-digit, unsigned binary number, or the left and right halves of a word can be taken as separate 18-bit numbers. The PDP–10 repertory includes instructions that add or subtract one from both halves of a word, so the right half can be used for address modification when the word is addressed as an index register, while the left half is used to keep a control count.

The fixed-point arithmetic instructions use twos complement representations to do binary arithmetic. In a word used as a number, bit 0 (the leftmost bit) represents the sign, 0 for positive, 1 for negative. In a positive number the remaining thirty-five bits are the magnitude in ordinary binary notation. The negative of a number is obtained by taking its twos complement. If x is an n-digit binary number, its twos complement is $2^n - x$, and its ones complement is $(2^n - 1) - x$, or equivalently $(2^n - x) - 1$. Subtracting a number from $2^n - 1$ (i.e. from all 1s) is equivalent to performing the logical complement, i.e. changing all 0s to 1s and all 1s to 0s. Therefore, to form a twos complement one takes the logical complement (usually referred to merely as the complement) of the entire word including the sign, and adds 1 to the result. In a negative number the sign bit is 1, and the remaining bits are the twos complement of the magnitude.

$$+153_{10} = +231_8 = \boxed{\texttt{000 000 000 000 000 000 000 000 000 010 011 001}}$$

0 35

$$-153_{10} = -231_8 = \boxed{\texttt{111 111 111 111 111 111 111 111 111 101 100 111}}$$

0 35

A twos complement addition actually acts as though the words represented 36-bit unsigned numbers, i.e. the signs are treated just like magnitude bits. In the absence of a carry into the sign stage, adding two numbers with the same sign produces a plus sign in the result. The presence of a carry gives a positive answer when the summands have different signs. The result has a minus sign when there is a carry into the sign bit and the summands have the same sign, or the summands have different signs and there is no carry. Thus the program can interpret the numbers processed in fixed point addition and subtraction as signed numbers with thirty-five magnitude bits or as unsigned 36-bit numbers. A computation on signed numbers produces a result that is correct as an unsigned 36-bit number even if overflow occurs, but the hardware interprets the result as a signed number to detect overflow. Adding two positive numbers whose sum is greater than or equal to 2^{35} gives a negative result, indicating overflow; but that result, which has a 1 in the sign bit, is the correct answer interpreted as a 36-bit unsigned number in positive form. Similarly adding two negatives gives a result which is always correct as an unsigned number in negative form.

Zero is represented by a word containing all 0s. Complementing this number produces all 1s, and adding 1 to that produces all 0s again. Hence there is only one zero representation and its sign is positive. Since the numbers are symmetrical in magnitude about a single zero representation, all even numbers both positive and negative end in 0, all odd numbers in 1 (a number all 1s represents −1). But since there are the same number of numbers with each sign and zero has a plus sign, there is one more negative number than there are strictly positive numbers (nonzero numbers with a plus sign). This is the most negative number and it cannot be produced by negating any positive number (its octal representation is 400000 000000 and its magnitude is one greater than the largest positive number).

If ones complements were used for negatives one could read a negative number by attaching significance to the 0s instead of the 1s. In twos complement notation each negative number is one greater than the complement of the positive number of the same magnitude, so one can read a negative number by attaching significance to the rightmost 1 and attaching significance to the 0s at the left of it (the negative number of largest magnitude has a 1 in only the sign position). In a negative integer, 1s may be discarded at the left, just as leading 0s may be dropped in a positive integer. In a negative fraction, 0s may be discarded at the right. So long as only 0s are discarded, the number remains in twos complement form because it still has a 1 that possesses significance; but if a portion including the rightmost 1 is discarded, the remaining part of the fraction is now a ones complement. Single precision multiplication produces a double length product, and the programmer must remember that discarding the low order part of a double length negative leaves the high order part in correct twos complement form only if the low order part is zero.

The computer does not keep track of a binary point — the programmer must adopt a point convention and shift the magnitude of the result to conform to the convention used. Two common conventions are to regard a number as an integer (binary point at the right) or as a proper fraction (binary point at the left); in these two cases the range of numbers represented by a single word is -2^{35} to $2^{35} - 1$ or -1 to $1 - 2^{-35}$. Since multiplication and division make use of double length numbers, there are special instructions for performing these operations with integral operands.

The format for double length fixed point numbers is just an extension of the single length format. The magnitude (or its twos complement) is the 70-bit string in bits 1–35 of the high and low order words. Bit 0 of the high order word is the sign, and bit 0 of the low order word is made equal to the sign. The range for double length integers and proper fractions is thus -2^{70} to $2^{70} - 1$ and -1 to $1 - 2^{-70}$. The double precision instructions actually use quadruple length numbers for products and dividends. But numbers of any length are just a further extension of the basic format: thirty-five additional bits of the number in each lower order word, and bit 0 made equal to the sign. Remember that truncating a multiple length negative requires an adjustment for the twos complement unless the part discarded is zero. The convention for bit 0 of lower order words is inconsistent with that used for floating point format (see below). This does not affect the arithmetic instructions themselves, as they ignore bit 0 in all lower order words. However instructions that negate a doubleword use the floating point convention. This means that if such instructions are used for fixed point numbers, a problem could arise when comparing one double precision number with another.

Floating Point Numbers

The floating point instructions provide for conversion between fixed and floating forms and handle both single and double precision floating point numbers. The same format is used for a single precision number and the high order word of a double precision number. A floating point instruction interprets bit 0 as the sign, but interprets the rest of the word as an 8-bit exponent and a 27-bit fraction. For a positive number the sign is 0, as before. But the contents of bits 9–35 are now interpreted only as a binary fraction, and the contents of bits 1–8 are interpreted as an integral exponent in excess 128 (200_8) code. Exponents from -128 to $+127$ are therefore represented by the binary equivalents of 0 to 255 ($0\text{–}377_8$). Floating point zero and negatives are represented in exactly the same way as in fixed point: zero by a word containing all 0s, a negative by the twos complement. A negative number has a 1 for its sign and the twos complement of the fraction, but since every fraction must ordinarily contain a 1 unless the entire number is zero (see below), it has the ones complement of the exponent code in bits 1–8. Since the exponent is in excess 128 code, an actual exponent x is represented in a positive number by $x + 128$, in a negative number by $127 - x$. The programmer, however, need not be concerned with these representations as the hardware compensates automatically. For example, for the instruction that scales the exponent, the hardware interprets the integral scale factor in standard twos complement form but produces the correct ones complement result for the exponent.

$$+153_{10} = +231_8 = +.462_8 \times 2^8$$

=

0	10 001 000	100 110 010 000 000 000 000 000 000
0	1 8	9 35

$$-153_{10} = -231_8 = -.462_8 \times 2^8$$

=

1	01 110 111	011 001 110 000 000 000 000 000 000
0	1 8	9 35

The floating point instructions assume that all nonzero operands are normalized, and they normalize a nonzero result. A floating point number is considered normalized if the magnitude of the fraction is greater than or equal to ½ and less than 1. The hardware may not give the correct result if the program supplies an operand that is not normalized or that has a zero fraction with a nonzero exponent.

Single precision floating point numbers have a fractional range in magnitude of ½ to $1 - 2^{-27}$. Increasing the length of a number to two words does not significantly change the range but rather increases the precision; in any format the magnitude range of the fraction is ½ to 1 decreased by the value of the least significant bit. In all formats the exponent range is −128 to +127.

The precaution about truncation given for fixed point multiplication applies to single precision floating point operations as they are done in extra length; but the programmer may request rounding, which automatically restores the high order part (the result) to twos complement form if it is negative. In double precision floating point instructions, all operands and results are double length, and all instructions calculate an extra length answer, which is rounded to double length with the appropriate adjustment for a twos complement negative. In double precision format the high order word is the same as a single precision number, and bits 1–35 of the low order word are simply an extension of the fraction, which is now sixty-two bits. Bit 0 of the low order word is made 0 in a result but is ignored in all operands; e.g. the number $2^{18} + 2^{-18}$ has this two-word representation in double precision format,

```
|0|10 010 011|100 000 000 000 000 000 000 000 000|
 0 1        8 9                                35

|0|00 000 000 010 000 000 000 000 000 000 000 000|
 0 1                                           35
```

and its negative is

```
|1|01 101 100|011 111 111 111 111 111 111 111 111|
 0 1        8 9                                35

|0|11 111 111 110 000 000 000 000 000 000 000 000|
 0 1                                           35
```

STANDARD MAGNETIC TAPE

A system for handling industry-standard magnetic tape consists of a TM10 control and up to eight tape transports; each unit in the system occupies a separate cabinet. DEC supplies several types of transports that differ in tape speed and tape handling characteristics. Each type is available in two versions, for recording information in seven tracks and nine tracks. Thus data transfer rates and timing depend on the transport, but each transport supplies information to the control such that transports of different speeds and recording formats can be operated by a single control. Transports currently available move tape at speeds of 45, 75 and 150 inches per second. Every transport accommodates two 10½-inch reels (one for supply, one for takeup) and can record information in three densities: 200, 556 and 800 bytes per inch (bpi). A full reel has 2400 feet of half-inch tape and at 800 bpi can store over 135 million bits of data in the 7-track format, or over 180 million bits in the 9-track format.

The program communicates with the tape control, which in turn governs all tape transports but communicates with only one transport at a time. Reading and writing (recording) can occur only when tape is moving forward (from supply reel to takeup reel), but the control can space the tape (*ie* move it to a new position) in either direction. Although only one transport can be reading, writing or spacing at a time, rewinding the entire tape onto the supply reel at high speed requires only initiation by the control. The rewinding transport then proceeds automatically while the control can operate another transport.

Data transfers between tape and control are governed entirely by the control. Transfers between a TM10A control and memory are handled by the program over the IO bus, whereas the TM10B control is connected to a data channel for automatic transfer of data to and from memory, thus bypassing the central processor [§5.1].

TAPE FORMAT

The control writes characters containing seven or nine bits of information; one bit is written in each track. Every character is part of a data record or a file mark. A data record contains both data characters and error-checking characters. Every data character consists of a data byte and a lateral parity bit, which the control generates so that the number of 1s in the character is odd or even as specified by the program. The data bytes in a record taken together correspond to a block of words sent from memory to the control. To separate adjacent records the control automatically erases a segment of tape between them; this segment is called a "record gap". The control always stops the tape in a gap.

The recording technique used is NRZI (nonreturn to zero, inverting). In a given frame (*ie* character position) a change in the direction of magnetization in any track represents a 1 in the character bit corresponding to that track. Thus if the same bit is 0 in a string of characters, there is no change in the track corresponding to that bit; but for a string of 1s, the flux direction changes in every frame.

To facilitate tape processing, the program can group sets of data records into files. The end of a file is indicated by a 3-inch gap followed by a file mark. The file mark is a special record containing a single, special data character and its LPCC, which is equivalent. The control always terminates a function when it encounters a file mark; in particular, the control can space by files as well as by numbers of records.

Each tape has two physical markers to indicate its extremities. These markers are reflective strips that are sensed by photoelectric cells in the transport (one marker can be seen on the tape in the illustration at the end of §H4.2). The loadpoint marker is located about fifteen feet in from the beginning of the reel and denotes the logical beginning of the tape. Reverse functions stop automatically at this marker. A load point gap of at least three inches (twenty-five feet maximum) precedes the first record on the tape. The endpoint marker is about twenty-five feet from the physical end of the tape; the final fifteen feet of tape should be left for trailer, *ie* the program should not record more than ten feet beyond the endpoint (this is enough for a 4000-word record at low density). A status bit indicates when the tape is beyond the endpoint, but this condition stops the tape automatically only when it is spacing forward.

Tapes recorded on some IBM transports have a substandard loadpoint gap of only .5 inch and are thus not compatible with the TM10.

The markers are on the shiny side of the tape; the endpoint marker is against the edge nearer the transport, the loadpoint marker is against the opposite edge.

An annular groove is molded into the back of every reel, and the control cannot write on the tape unless the supply reel has a plastic (write enable) ring in this groove. By leaving the ring out, the operator can protect the data on the tape from accidental destruction (overwriting or erasure).

While the control is actually processing the data portion of a record, the data transfer rate is fixed. However, in a lengthy tape run, the effective (average) transfer rate depends on record length, which determines the percentage of tape taken up by gaps (at the highest density in 7-track format, each record gap could hold 100 additional words). The effective transfer rate is therefore a function of record length as well as tape speed and density.

Full words are transferred between memory and control even though the tape characters may contain 6-bit or 8-bit data bytes. To write, the control divides the words into data bytes, and when reading, the control reassembles the bytes into words. There are several ways in which this is done. For 7-track format, the program can select any density, and the control writes each word as six characters, each containing a 6-bit data byte. After the control writes the last data character for a record, it writes three blank frames (zero characters) followed by a longitudinal parity check character (LPCC). The three blank frames constitute the end of record gap (EOR), which is used by the control to detect the end of record. The EOR is used in writing as well as reading since the tape encounters the write head first, and the control detects everything shortly after writing it. The LPCC (which may be zero) produces even parity in each of the tracks along the length of the record. The minimum record gap is .75 inch.

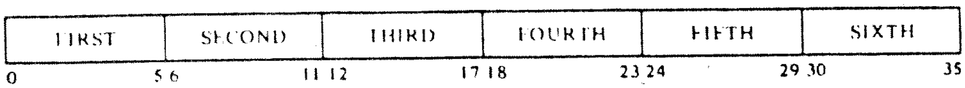

7-TRACK BYTE DISTRIBUTION

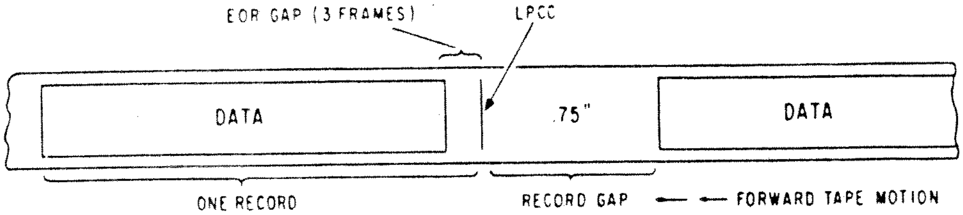

7-TRACK RECORD FORMAT

When the control reads or writes a data record, it checks that the (lateral) parity of every data character agrees with the parity specified by the program and checks that every track has even (longitudinal) parity.

The 9-track format is used for recording data compatible with systems based on 8-bit bytes. The program must select a density of 800 bpi, and the control writes bits 0–31 of each word in four characters, ignoring bits 32–35 altogether. The bits from left to right in each 8-bit byte are written in tracks 0–7. After writing the last data character, the control writes an EOR gap, a cyclic redundancy character (CRC), three more blank frames, and an LPCC. The control generates the CRC as described in §6 of USAS X3.22-1967, *USA Standard, Recorded Magnetic Tape for Information Interchange* (*800 CPI, NRZI*). Taking the CRC bits as numbered in that document and the track scheme defined above, CRC bit 1 corresponds to the parity track and bits 2–9 correspond to tracks 0–7. The standard record gap is .5 inch minimum, .6 inch nominal, 25 feet maximum.

For industry compatibility the program must select 800 bpi and odd parity.

The difference in nominal gap length between 7-track and 9-track format is due entirely to a difference in head spacing.

When the control reads a record in 9-track format, it assembles data into 36-bit words. Each word is composed of four data bytes in bits 0–31 and the corresponding character parity error indicators in bits 32–35 (*eg* a 1 in bit 33

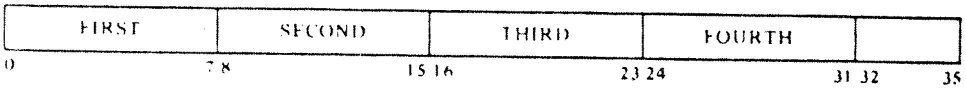

9-TRACK BYTE DISTRIBUTION

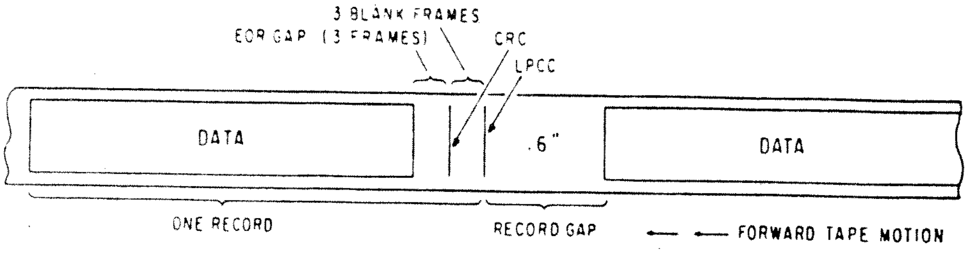

9-TRACK RECORD FORMAT

indicates an error in the character from which the byte in bits 8–15 was taken). If errors occur, the program can use the cyclic redundancy character to determine if the errors are confined to a single track, and if so, to correct them. After reading the data characters in a record, the control makes the CRC available in a word in which bits 0–7 contain information from the data tracks and bit 32 contains a parity error bit. The program can correct errors by using the procedure described in Appendix B of the standard. It is not necessary to reread the tape: the error pattern can be generated from the data in memory. If errors are confined to a single track, the program can correct the record by complementing the bit from the bad track in every byte whose error bit is 1.

To facilitate the use of 9-track tape for binary data applications, a core dump format is available in which the program can select any density, and the control uses the 9-track record format but writes full 36-bit words as five characters each. The first four bytes are taken from bits 0–31 of a word in the same manner as in 9-track format; the fifth data byte contains 0s in tracks 0 and 1 and bits 30–35 of the word are contained in tracks 2–7. To reassemble the word during reading, the control ors the overlapping bits. The CRC is written in the usual fashion, but no error bits are supplied with the data bytes.

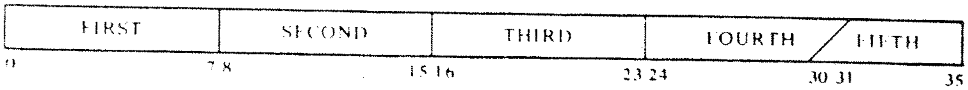

CORE DUMP BYTE DISTRIBUTION

When writing in even parity in any recording format, the program must not supply a word containing a zero data byte, since this would result in a missing character (a blank frame), and no words beyond that point would be reassembled correctly. The control does not check for missing characters when reading, but such an event always terminates the function at the end of the current record.

Characters are assembled into words in this manner by an IDPB loop or an ASCII or ASCIZ pseudoinstruction.

The "tracks" referred to here are simply a convenience for identifying the bits in the data bytes. The actual correspondence of character bits to physical tracks on tape is as follows.

BIT	2	0	4	P	5	6	7	1	3
TRACK	1	2	3	4	5	6	7	8	9

This scheme, which minimizes the effects of errors, is recommended in the standard referenced in the text.

A 1 in an error bit does not necessarily mean the corresponding byte is in error: the error could be in the parity track.

The program must use bit 32 and the parity being checked for in order to regenerate the bit actually read from the parity track of the CRC by the control, keeping in mind that the parity track does not contain an actual parity bit. The parity of the CRC will be odd if the number of data characters in the record is even, otherwise the CRC parity is even.

Errors discovered in a record in core dump format at 800 bpi can be corrected by rereading the record in 9-track format, if investigation of the CRC indicates the errors are confined to a single track. The program must then reconstruct the original words, four from each group of five 4-byte sets supplied by the control.

Two or more contiguous missing characters would be interpreted by the control as an EOR gap. This sets the Bad Tape flag and terminates the function.

Description of the data on the tape

The data consist of two parts:

1.) the active time of the experiment

2.) the scientific results (micrometeoroid impact data)

1.) We have four different active times, in fractions of the total available time, namely for

a) protected data, amplitude range 1

b) unprotected data, amplitude range 1

c) protected data, amplitude ranges 2,3,4

d) unprotected data, amplitude ranges 2,3,4

(for correlation with the data see word 20 and 21 of the scientific data)

The data start with day 349/1974 and end with day 181/1980.

We always took the average of 10 days.

So you have 203 records with respectively 4 words.

2.) For each of the 235 particles we have one record with 47 words.

We only used floating point numbers.

Meaning of the words:

word 1: number of particle

word 2: event-time year

word 3: event-time day of year

word 4: event-time hour

word 5: event-time minute

word 6: event-time second

word 7: 0. if the impact was on the Ecliptic-Sensor
1. if the impact was on the South-Sensor

word 8: lower limit velocity (1-σ)

word 9: most probable impact velocity

word 10: upper limit velocity (1-σ)

word 11: lower limit mass (1-σ)

word 12: most probable particle mass

word 13: 1. if the given mass is a lower limit (overflow data)
0. otherwise

word 14: upper limit mass (1-σ)

word 15: distance to sun (AU) at the time of the impact

word 16: true anomaly of HELIOS 1 at the time of the impact

word 17: sensor azimuth signifies the projected direction of the sensor axis to the ecliptic (90^0 is the direction to sun, 0^0 is perpendicular to the sun in direction of the apex of HELIOS 1)

word 18: 1. if true anomaly and sensor azimuth indicate an eccentric orbit ($e>0.$)
0. otherwise

word 19: total charge in the mass spectrum ($\sim 10^{-13}$ C)

word 20: Q_I-amplitude range

word 21: 1. for protected data
0. for unprotected data

word 22: meanvalue of the reciprocal semi-major axis

word 23: standard-derivation of the reciprocal semi-major axis

word 24: meanvalue of the eccentricity

word 25: standard-derivation of the eccentricity

word 26: meanvalue of the inclination

word 27: standard-derivation of the inclination

word 28: meanvalue of the perihel distance (AU)

word 29: standard-derivation of the perihel distance (AU)

word 30: probability for inbound (≥ 0.75) and outbound (≤ 0.25) trajectory at the moment of the impact. $0.25 <$ word $30 < 0.75$ means that the particle was registered near his perihel or aphel. (c.f. K.D.Schmidt and E.Grün, 1979,1980)

word 31: probability of hyperbolic orbit ($e > 1$). A hyperbolic orbit is given, if word $31 \geq 0.75$

word 32: shows, for which radiation pressure model (c.f. K.D.Schmidt and E.Grün,1979,1980) the particle has a hyperbolic orbit (word $31 \geq 0.75$)
0. if the particle has a hyperbolic orbit for the models 0,1 and 2
1. if the particle has a hyperbolic orbit for the models 1 and 2
2. if the particle has a hyperbolic orbit only for model 2
3. for no radiation pressure model is word $31 \geq 0.75$

word 33: 1. indicates an overflow of the positiv impact charge Q_I
0. otherwise

word 34: 1. density of eccentric particles (word 18) smaller than 0.1 g/cm^3 (c.f. N.Pailer and E.Grün, 1980 and Grün et al, 1980)
0. otherwise

word 35: chemical classification
1. if undefined spectrum
2. if chondritical spectrum
3. if ironrich spectrum

word 36-47: mass spectrum. The amount of ions is given for 12 massranges from 16 amu to 74 amu. The total amount of ions is normalized to 1 for the massrange 16 amu to 74 amu.

Summary of the organisation of the data on tape:

There are 438 records on tape.

The first 203 records with respectively 4 words (active time).

The last 235 records with respectively 47 words (scientific data).

Further details on the data can be obtained from

E.Grün
Max-Planck-Institut für Kernphysik
Saupfercheckweg 1
D-6900 Heidelberg
Federal Republic of Germany

References

1 "The Distribution of Orbital Elements of Interplanetary Dust in the Inner Solar System as Detected by the Helios Spaceprobe", K.D.Schmidt and E.Grün, Space Research XIX, ed. M.J.Rycroft, Pergamon Press, Oxford and New York, S. 439-442 (1979).

2 "Orbital Elements of Micrometeoroids Detected by the HELIOS 1 Space Probe in the Inner Solar System", K.D.Schmidt and E.Grün, Proceeding of IAU Symposium 90, eds. I.Halliday and B.A.McIntosh, in "Solid Particles in the Solar System", eds. I.Halliday and B.A.McIntosh, S. 321-324 (1980).

3 "The Penetration Limit of Thin Films", N.Pailer and E.Grün, Planet. Space Sci., Vol. 28, S.321-331 (1980).

4 "Orbital and Physical Characteristics of Micrometeoroids in the Inner Solar System as Observed by Helios 1", E.Grün, N.Pailer, H.Fechtig and J.Kissel, Planet. Space Sci., 28, S.333-349 (1980).

B33268-02UA
74-097A-12A
DSC #514

THE DISTRIBUTION OF ORBITAL ELEMENTS OF INTERPLANETARY DUST IN THE INNER SOLAR SYSTEM AS DETECTED BY THE HELIOS SPACE-PROBE

K.D. Schmidt* and E. Grün**

Ruhr-Universität Bochum, Bereich Extraterrestrische Physik, Bochum, FRG
***Max-Planck-Institut für Kernphysik, Heidelberg, FRG*

INTRODUCTION

On board the Helios Space-probe there are two micrometeoroid detectors (Experiment E 10) [1]. Viewing both in the ecliptic plane und southwards, these are able to detect dust particles along the spacecraft's orbit around the sun [2,3]. The orbit has its perihelion at 0.3 A.U., an aphelion at 1 A.U. and an eccentricity of 0.52. Therefore Helios allows us to obtain direct information about the interplanetary dust cloud in the inner regions of the solar system.

Here we are interested in the osculating orbital elements (semimajor axis a, eccentricity e, inclination i) of dust particles detected during the first 6 orbits of Helios 1. The mass range of the particles detected is 10^{-17}g to 10^{-6}g. Since data reduction of the measurements is still going on, the work up to now is restricted to results obtained by analysis of about 168 recorded particles.

PROBABILITY DISTRIBUTION OF ORBITAL ELEMENTS OF A PARTICLE

The orbital elements of each particle are derived by transforming the impact speed observed in the respective viewing direction of the sensor into a heliocentric dust velocity. Since the viewing cone is large, uncertainties in impact direction occur. Therefore about 200 possible impact directions compatible with the observation were chosen at random within the field of view for each particle. Taking into account the sensors' intrinsic sensitivity for different impact angles, weighted heliocentric dust velocities were derived [4]; with the known position at impact the weighted orbital elements were also derived.

For each single impact (e.g., particle No. 137) the probability for a certain range of semimajor axes, eccentricities, and inclinations is plotted in histograms (e.g. Fig. 1). Since particles in the observed mass range usually undergo radiation pressure this effect on those distributions also is taken into account. The parameter ß, which is the ratio of the force of radiation pressure (F_{rad}) and the gravitational force of the sun (F_{grav}) here is chosen as $F_{rad}/F_{grav} = 0.4$. Without radiation pressure, for example, particle No. 137 has an elliptic, i.e. bounded orbit. Since radiation pressure shifts the semimajor axis and eccentricities to higher values there is a certain probability w that the particle is on a hyperbolic orbit ($e > 1$). For particle No. 137 this probability is 0.122, whereas for other particles w may be 1 even without radiation pressure. Particle No. 137 was on a prograde orbit with possible inclinations lying between 0° and 18°.

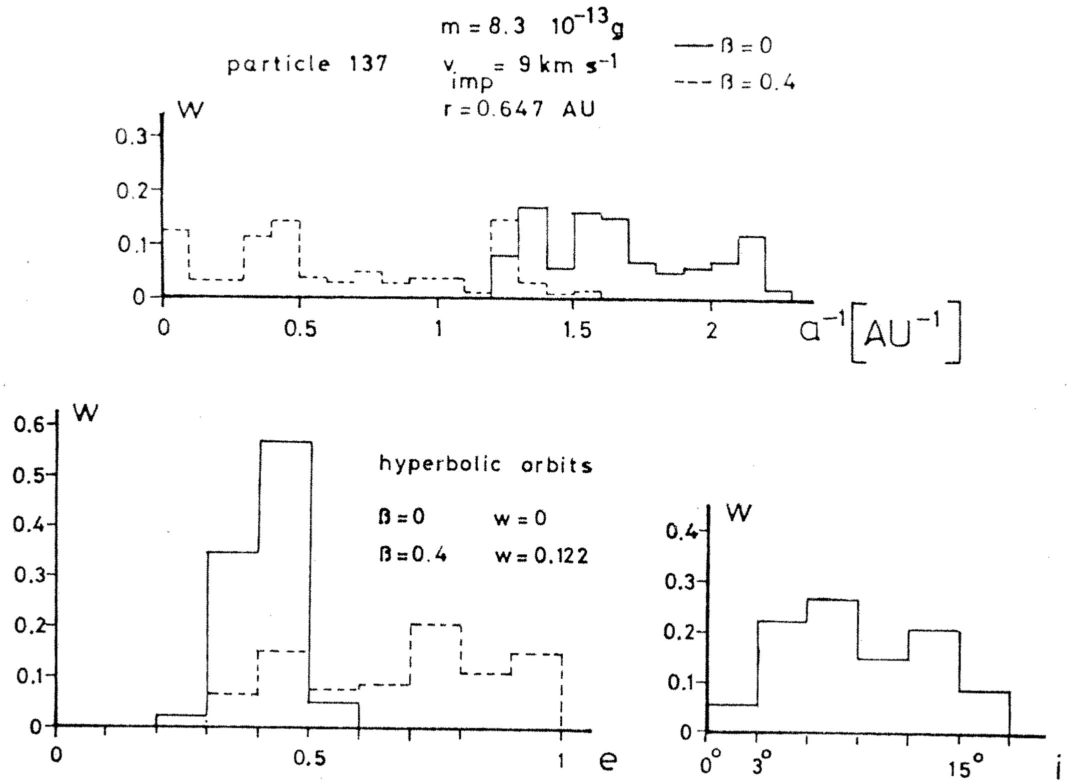

Fig. 1 Probability-distributions of orbital elements for one mocrometeoroid (No.137).

ORBITAL ELEMENTS OF GROUPS OF PARTICLES

Since detailed information on impact velocity is available only up to an impact velocity of about 50 km s^{-1}, the detected particles were divided into two groups for each detector. The first group corresponds to $0 \leq V_{imp} < 50$ km s^{-1} and the second one with $V_{imp} \geq 50$ km s^{-1}. This separation is approximately equivalent to a division in masses of dust particles where $m > 10^{-11}$g applies for the first group and $m < 10^{-11}$g for the second one, because the measurable mass is a function of the particle's velocity [1]. The histograms of the individual particles in one group were added and normalized to obtain probability distributions in 1/a, e, and i for each group.

Two examples are presented here. The first (Fig. 2) refers to larger particles ($m > 10^{-11}$g) detected by the south viewing sensor. The second example (Fig. 3) presents the case of smaller particles ($m < 10^{-11}$g) as observed by the ecliptic sensor. Other cases are similar to those examples. The effect of constant radiation pressure for each mass is shown, although this effect also depends on the particles shapes and chemical composition. Nevertheless qualitatively the way in which radiation pressure influences the orbital element distribution is well demonstrated. Particles characterized by high eccentricities $e > 1$ are on hyperbolic orbits and will leave the solar system. Therefore these particles were not further distinguished in their orbital elements, like the bounded ones ($e < 1$), except for their inclination which is not affected by radiation pressure. Fig. 4 shows that the larger particles are more concentrated in the ecliptic plane than smaller particles ($m < 10^{-11}$g). Both groups show only a negligible probability of retrograde orbits: these probabilities are 0.15 and 0.0 for the ecliptic and for the south viewing sensors, respectively.

These first results which suggest the existence of particles in hyperbolic orbits and significant differences in dynamical properties between at least two groups of observed particles stimulate the evaluation of further Helios results in order to establish realistic boundary conditions for modelling the dynamics of the interplanetary dust cloud.

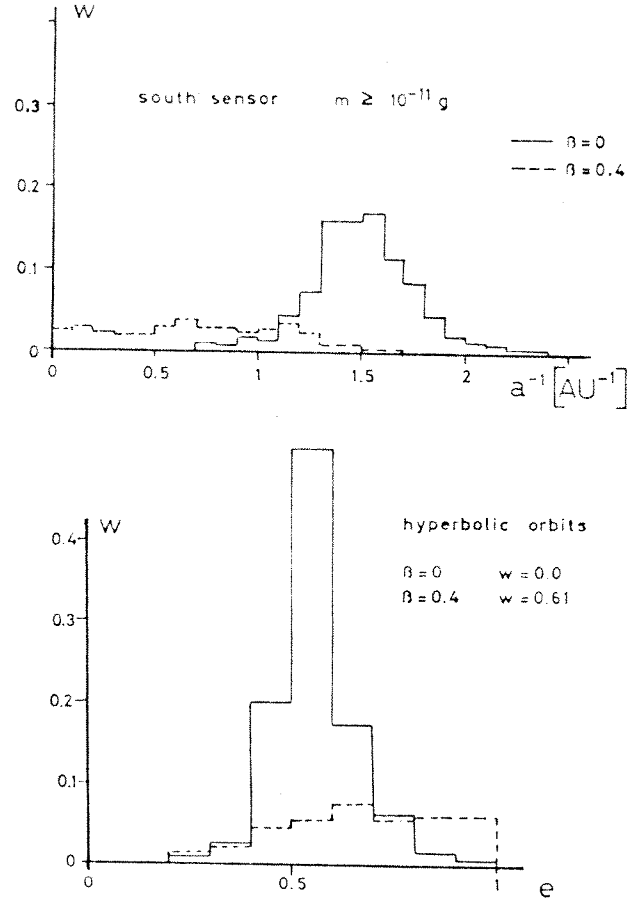

Fig. 2 Probability-distributions of orbital elements for micrometeoroids with $m > 10^{-11}$ g.

REFERENCES

1. H. Dietzel, G. Eichhorn, H. Fechtig, E. Grün, H.-J. Hoffmann, J. Kissel, *J. Phys. E.: Sc. Inst.* 6, 209 (1973).
2. E. Grün, H. Fechtig, J. Kissel, P. Gammelin, *J. Geophys.* 42, 717 (1977).
3. E. Grün, J. Kissel, H. Fechtig, P. Gammelin, J.H. Hoffmann, *Lecture Notes Phys.* 48, 159, Springer Berlin-Heidelberg-New York, 1976.
4. K.D. Schmidt, *J. Geophys.* 42, 737 (1977).

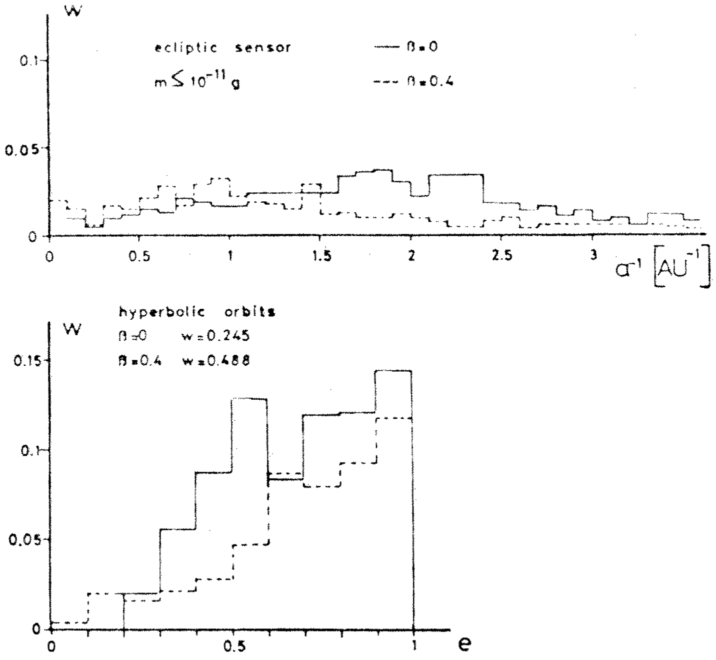

Fig. 3 Probability-distributions of orbital elements for micrometeoroids with $m < 10^{-11}$g.

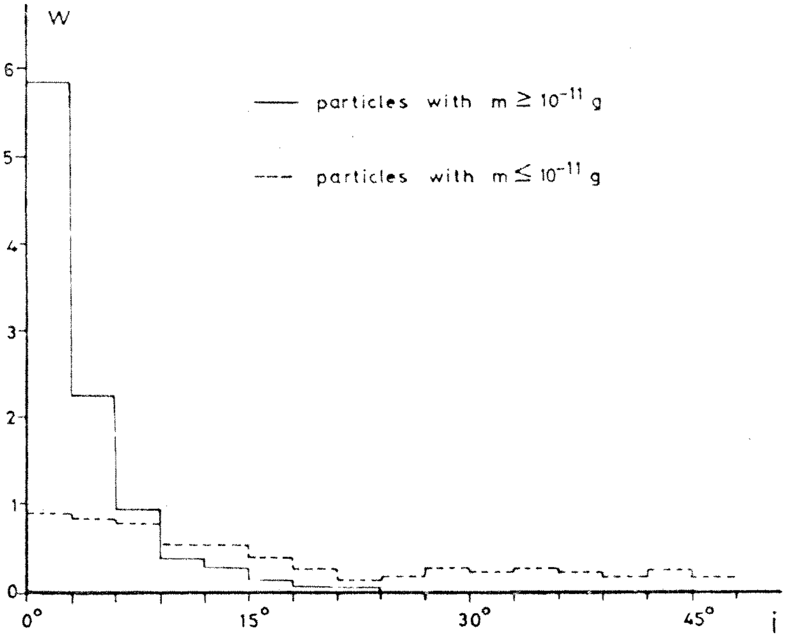

Fig. 4 Probability-distributions of the inclinations for two groups of particles corresponding to Fig. 2 and Fig. 3.

ORBITAL ELEMENTS OF MICROMETEOROIDS DETECTED BY THE HELIOS 1 SPACE PROBE IN THE INNER SOLAR SYSTEM

K.D. Schmidt
Ruhr-Universität Bochum, Bereich Extraterrestrische Physik

E. Grün
Max-Planck-Institut für Kernphysik, Heidelberg, Germany

The Helios Spacecraft is able to detect micrometeoroids along its orbit in the inner Solar System between 0.3 AU and 1 AU distance from the sun (Grün et al. 1977, Grün et al. 1979). Data of the first 6 orbits are presented here. 168 particles have been identified in such a way that their osculating orbital elements (here especially semimajor axis a, eccentricity e and inclination i) can be calculated. Detailed information on impact speed is available only up to about 50 km s^{-1} which corresponds to a lower mass limit of 10^{-11}g (Dietzel et al. 1973). So the detected micrometeoroids are divided into two groups below and above 10^{-11}g for each sensor. Table 1 gives the absolute number of dust particles in the different mass intervals.

Table 1 Identified particles of the first 6 orbits of Helios 1

	Sensor	
Mass (g)	**South**	**Ecliptic**
$< 10^{-11}$	73	29
$> 10^{-11}$	43	23

The particles in the observed mass ranges are influenced in their orbital motion by radiation pressure. Therefore mass-dependent models of radiation pressure were taken into account. The models used a mixture of materials in proportions to represent the optical properties of the zodiacal dust cloud according to Röser and Stauda (1978). One model includes absoring materials (graphite), the other has none. Above 10^{-11}g there is not a great difference

I. Halliday and B. A. McIntosh (eds.), Solid Particles in the Solar System, 321–324.

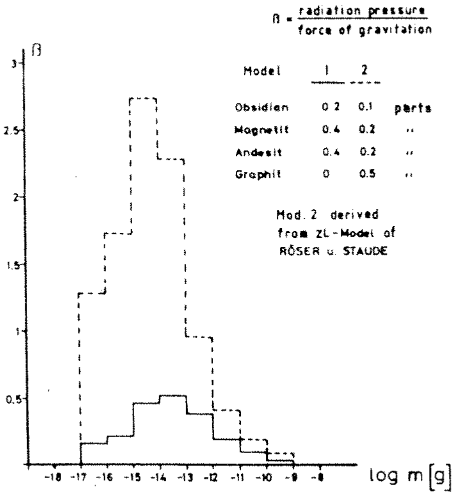

Figure 1 Mass dependent radiation-pressure models.

in the models so that the orbits of large particles are not affected by the choice of model. Depending on the velocity at the time of creation, ß-values below 1 may be enough to blow particles out of the Solar System. From this point of view the two models may be considered as upper and lower limits of radiation pressure, until we know the detailed optical properties of the particles.

The uncertainties in impact speed and impact direction (due to the large viewing cones of the micrometeoroid sensors) forced us to calculate many possible dust velocities for each single particle (Schmidt and Grün 1979). Taking into account sensor intrinsic weighting factors for different impact directions we computed probability distributions for the osculating orbital elements. In Fig. 2 an example of the probability p for a single particle to be in a certain orbital element interval is given. Since particles on unbound (hyperbolic) orbits are leaving the Solar System, the probabilities for the different hyperbolic orbits are given as a sum (p_{hyp}). For particle no. 137 the total probability for hyperbolic orbits is 24% if ß = 0.4, whereas all possible orbits are bound for ß = 0.0. Radiation pressure shifts 1/a to lower, e to higher values, but does not affect inclination. 98% of the detected particles were on prograde orbits. Fig. 3 shows the probabilities for groups of particles normalized to unity. Larger particles are not so much affected by the two different models of radiation pressure. These particles are nearly all on bound orbits.

The mass range of the larger particles corresponds to those which make the major contribution to the observed zodiacal light. The smaller particles which are in size ranges that do not contribute to the zodiacal light have high probabilities to be on hyperbolic orbits leaving the Solar System on their first orbit. Table 2 gives detailed information about these hyperbolic micrometeoroids, which were divided into three groups for each sensor, depending on the direction the

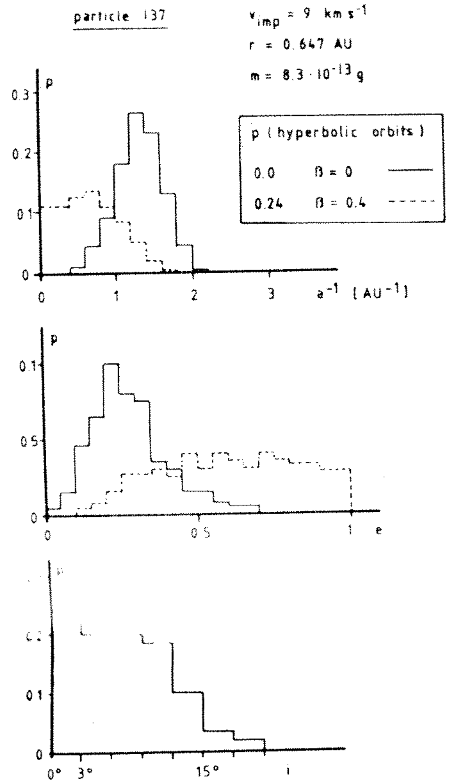

Figure 2 Probability distributions for a single particle.

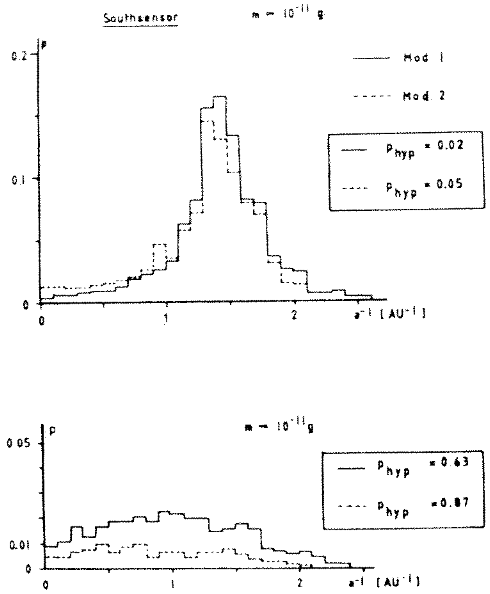

Figure 3
Probability distributions for groups of particles.

particles were going when they were detected. Under the above mentioned conditions of sensor characteristics and radiation pressure models, there were comparable numbers of particles travelling inward (toward the Sun) and outward. The difference in the counts for these two groups must be due to β-meteoroids produced inside the orbit of Helios. New results (Schwehm 1979) which show that melting and evaporation of dust grains near the sun is not a sufficient source for β-meteoroids, may explain the rather small number of β-meteoroids. A source for the incoming particles of small masses may be dust-dust collisions outside the orbit of Helios. The possible interstellar origin of these particles is doubtful due to the work of Morfill and Grün (1979), who concluded that the solar magnetic field may shield the inner Solar System from interstellar particles.

Table 2 Number of hyperbolic orbits

Southsensor	$\beta = 0$	Mod 1	Mod. 2
into the Solar System	8	11	17
out of the " "	7	21	26
detected close to perihelion	9	10	16
Eclipticsensor			
into the Solar System	0	1	9
out of the " "	2	5	11
detected close to perihelion	0	0	4

The results of this analysis suggest that at least two different groups of particles in the mass range of 10^{-6}g to 10^{-15}g exist, inferred from their dynamical behaviour. One group has masses greater than 10^{-11}g, moves on bound orbits and contributes to the zodiacal light, the other group consists of small grains with masses less than 10^{-11}g moving on hyperbolic orbits.

REFERENCES

Dietzel, H., Eichhorn, G., Fechtig, H., Grün, E., Hoffmann, H.J., Kissel, J.: 1973, J. Phys. E.Sc.Inst. 6, p. 209.

Grün, E., Fechtig, H., Kissel, J., Gammelin, P.: 1977, J. Geophys.42, p. 717.

Grün, E., Pailer, N., Fechtig, H., Kissel, J.: 1979, submitted to Planet. Space Sci.

Morfill, G. and Grün, E.: 1979, to be published in Planet.Space Sci.

Röser, S. and Staude, H.J.: 1978, Astron. Astrophys. 67, p. 381.

Schmidt, K.D. and Grün, E.: 1979, M.J. Rycroft (ed.) Space Res. XIX, Pergamon Press Oxford and New York, p. 439.

Schwehm, G.: 1979, 'Temperaturverteilung und Dynamik interplanetarer Staubteilchen in der Nähe der Sonne', Ruhr-Universität Bochum (Ph.D.Thesis).

SUMMARY OF DISCUSSION

The conclusion that most large particles are on bound orbits is in conflict with Fried's (1978 Astron. Astrophys. *68*, pp. 259-264) observation of higher orbital velocities seen in the Doppler shift of solar absorption lines in the zodiacal light. Although particle speed is determined by Helios only within a factor of two, this is still accurate enough in many cases to discriminate between bound and hyperbolic orbits. The high line-of-sight velocities implied by Fried's observations cannot be produced by any known forces.

-3-

B33270-

74-097A-12A

DSC #514

Planet. Space Sci. Vol. 28, pp. 321–331. Pergamon Press Ltd., 1980. Printed in Northern Ireland

THE PENETRATION LIMIT OF THIN FILMS

N. PAILER, and E. GRÜN
Max-Planck-Institut für Kernphysik, Postfach 10 39 80, 6900 Heidelberg F.R.G.

(*Received* 22 *October* 1979)

Abstract—One sensor of the Helios micrometeoroid experiment is covered by a thin film consisting of 3000 Å parylene and 750 Å aluminium. Micrometeoroids must penetrate this film before they are detected. In order to study the effects of the film on the detection of micrometeoroids simulation experiments were performed with iron, aluminium, glass and polyphenylene projectiles in the mass range of $5\times10^{-13}\,\mathrm{g} < m < 2\times10^{-10}\,\mathrm{g}$ and in the speed range of $1.5\,\mathrm{km/sec} < v < 13\,\mathrm{km/sec}$. The bulk densities of the projectiles ranged from $1.25\,\mathrm{g/cm^3}$ (polyphenylene) to $7.9\,\mathrm{g/cm^3}$ (iron). By measuring the speed of the projectiles before and after the film penetration the speed loss Δv caused by the film was determined. The angle of incidence was varied in three steps (0°, 30° and 60°). This deceleration strongly depends on the projectiles' densities: Vertically impacting iron projectiles of $m = 10^{-11}$ g and $v_1 = 3$ km/sec were subject to a relative speed loss of $\Delta v/v_1 = 4\%$, aluminium projectiles of the same mass and speed showed $\Delta v/v_1 = 8\%$, glass projectiles $\Delta v/v_1 = 9\%$ and polyphenylene projectiles $\Delta v/v_1 = 14\%$. The total charge of the plasma produced upon impact on a gold target of a projectile which had penetrated the film before that was compared with the plasma produced by a projectile without a penetration. For iron projectiles these two signals did not differ significantly even at an angle of incidence of 60°. Whereas polyphenylene projectiles showed an attenuation of the charge signal by a factor of 10 after the penetration already at an angle of incidence of 0°. Polyphenylene projectiles impacting the film at an angle of incidence of 60° could no longer be detected behind the film. This experiment defined the penetration limit of the Helios film. Comparison with other penetration data yielded a penetration formula which is applicable to projectiles with diameters in the submicron to centimeter range. This penetration formula gives the penetration limit of a film as a function of the projectile's mass, speed and density.

1. INTRODUCTION

Direct information on micrometeoroids is obtained by *in situ* detectors on board of satellites and spaceprobes. Due to the low impact rate (of the order of 1 impact per week) of interplanetary dust particles onto these sensors measures have to be taken in order to prevent false impact identification by interference from the interplanetary medium or by noise generated on board the spacecraft itself. Thin films are used in micrometeoroid experiments to shield external noise sources from the sensors and to provide coincident signals upon penetration of dust particles (Berg and Richardson, 1969). The use of a film in such an experiment affects its data because small dust particles are "cut-off" from detection. This has been observed e.g. by the Pioneer 8 and 9 cosmic dust experiments (Berg and Grün, 1973) and the Helios micrometeoroid experiments (Grün *et al.* 1979). Laboratory simulations of penetration effects have been published previously (Grün and Rauser, 1969, Naumann *et al.* 1969 and McDonnell, 1970) but they are not directly applicable to every space experiment. Therefore an extensive simulation program has been started in order to determine the penetration effects on dust particles by the film which is used in the Helios micrometeoroid experiment. The micrometeoroid experiment on board Helios detects individual dust particles by the plasma produced upon impact onto the sensors. The experiment consists of two sensors. One sensor (south sensor) is facing the southern ecliptic hemisphere and detects particles with trajectory elevations from −90° to −4° with respect to the ecliptic plane. The other sensor (ecliptic sensor) detects particles with elevations from −45° to +55°. Because the spacecraft spins about an axis which is perpendicular to the ecliptic plane, the ecliptic sensor is periodically exposed to the sun. In order to avoid interference from sunlight, UV-radiation and solar wind particles, this sensor had to be protected by a thin entrance film, consisting of 3000 Å parylene coated with 750 Å aluminium. The south sensor is shielded from solar emissions by the spacecraft rim and therefore has an open aperture.

Calibration of the Helios experiment carried out at the Heidelberg dust accelerator using iron projectiles, showed no difference in the sensitivity of both sensors. On the other hand the impact rates of micrometeoroids onto both sensors measured during flight showed big differences: the south sensor detected approximately twice as many impacts as the ecliptic sensor (Grün *et al.* 1977 and Grün *et al.* 1980). This fact conflicts with the general result from zodiacal light observation (e.g. Leinert *et al.* 1977), namely that the dust is concentrated towards the ecliptic plane and also contradicts results predicted from meteor observations (Southworth and Sekanina, 1973), which indicate a predominance of low inclination orbits. Grün *et al.* (1980) showed that for an orbit inclination distribution similar to the meteor inclination distribution at least equal numbers of impacts should be detected by both sensors. Therefore, the observed difference in the number of impacts is due to the only difference between the sensors, namely the entrance film in front of the ecliptic sensor.

In this paper results from simulation experiments are presented showing a strong dependence of the penetration limit on the projectile densities. These results are used (Grün *et al.* 1980) in order to explain the observed effect in the Helios data. Firstly, results from deceleration experiments are given, then the penetration limit of the Helios film is determined. Lastly, the Helios results are compared with results from other penetration studies and an amended penetration formula is derived.

2. DECELERATION BY FILM PENETRATION

Dust projectiles are detected by an impact plasma detector if their impact speed exceeds approximately 1 km/sec (Dietzel *et al.* 1973). If dust projectiles are decelerated upon film penetration below this speed limit, they will not be detected and the effect is the same as if they were completely stopped by the film. Interest in the limits of detection under these conditions led to a study of the deceleration of high speed projectiles passing through a thin film. Projectiles consisting of iron, aluminium, glass and polyphenylene were used for these experiments. Table 1 gives a compilation of projectile parameters. Figure 1 shows the experimental set-up used for the measurement of the particle speed in front and behind the foil consisting of two time-of-flight paths of equal length $s_o = 66.5$ cm. They are separated by a sample of the Helios film (deceleration measurement) or by a grid in place of the film (calibration). The film can be rotated about an axis perpendicular to the flight direction in order to simulate inclined incidence directions.

TABLE 1. PROJECTILES FOR PENETRATION STUDIES

Projectile material	Density (g/cm^3)	Mass range (g)	Speed range (km/sec)
Iron	7.85	2×10^{-10}–5×10^{-13}	1.4–13.3
Aluminium	2.7	4×10^{-11}–2×10^{-12}	3.0– 7.5
Glass	2.4	2×10^{-10}–6×10^{-12}	1.5– 4.2
Polyphenylene	1.25	5×10^{-11}–3×10^{-13}	2.0–11.0

The first time mark is taken from a cylindrical detector (faraday cup) on which the highly charged dust projectile induces a signal proportional to its charge. This signal starts at the time when the projectile enters the cylinder. It triggers a 100 MHz oscillator. The flight distance from the entrance grid of the cylindrical detector to the grounded grid in front of the film is 66.5 cm. As soon as the projectile passes through the grid, which is mounted 1 mm in front of the Helios film, it induces a charge pulse on this film. This signal is the stop mark for the first speed measurement v_1 in front of the foil. Additionally, it is the first time

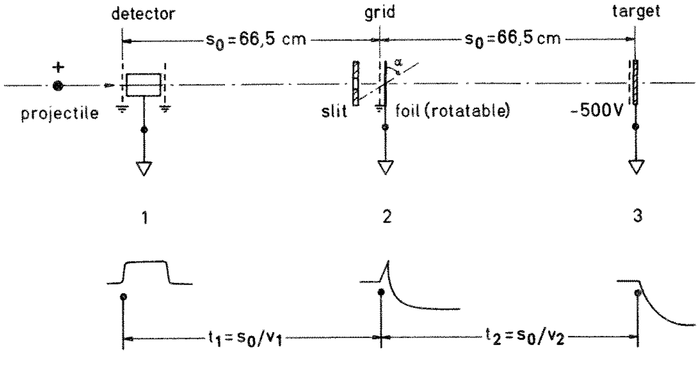

FIG 1. EXPERIMENTAL ARRANGEMENT (SCHEMATIC) OF THE MEASUREMENT OF THE DECELERATION BY FILM PENETRATION

Top: mechanical configuration. Bottom: derived signals.

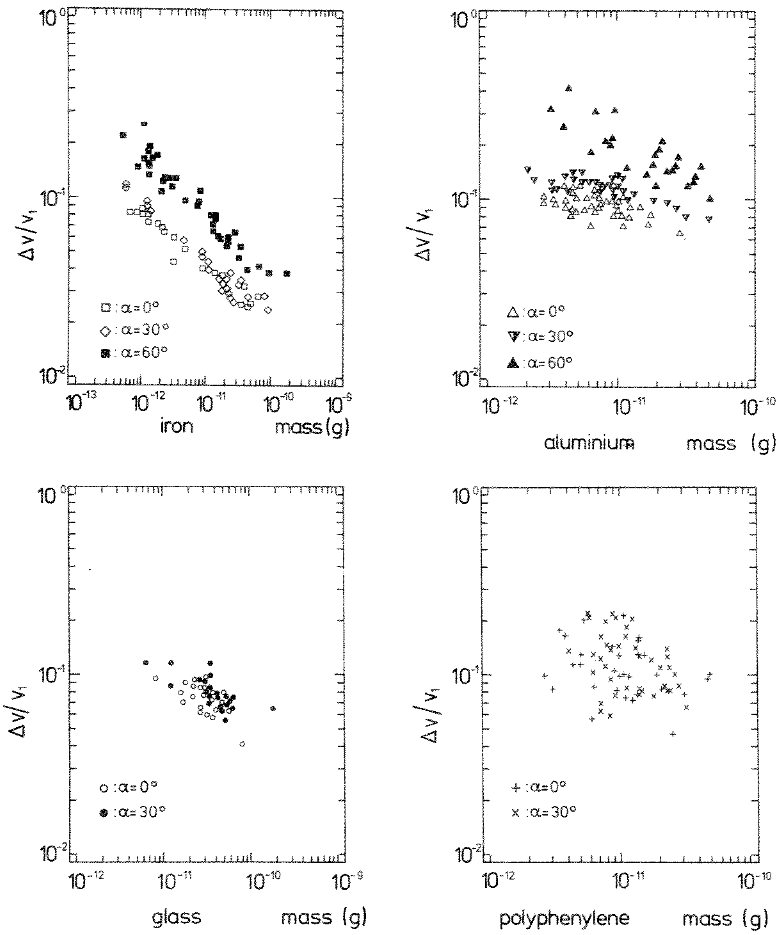

FIG 2. THE RELATIVE VELOCITY LOSS $\Delta v/v_1$ VERSUS THE MASS m OF DIFFERENT PROJECTILES.

mark for the speed measurement v_2 behind the film. The third mark is given by an impact ionisation detector, which is mounted at the end of the second time-of-flight path. When a projectile hits the gold target, an impact plasma is produced. The electrons of the plasma are collected by the target and generate the third time mark.

The results of the deceleration measurements are shown in Fig. 2. The relative velocity loss $\Delta v/v_1 = (v_1 - v_2)/v_1$ is plotted versus the projectile mass. It should be noted that, due to the characteristics of the dust accelerator (Fechtig *et al.* 1978), the masses of dust projectiles at a given speed vary only by a factor of approx. 10. In addition to that there is a correlation between the average mass and the speed of the accelerated dust projectiles of the form $m \sim v^{-4}$ (i.e. fast dust projectiles are generally small, while slow projectiles have large masses). The magnitude of the deceleration is correlated with the projectile density. Iron projectiles of $m = 10^{-11}$ g and $v = 3$ km/sec, which impact perpendicular to the film are decelerated by $\Delta v/v_1 \sim 4\%$, aluminium projectiles of the same mass and speed by 8%, glass projectiles by 9% and polyphenylene projectiles by 14%.

At an angle of incidence of $\alpha = 60°$ iron projectiles of $m = 10^{-10}$ g were decelerated by 4%, projectiles with $m = 10^{-11}$ g by 9% and projectiles with $m = 10^{-12}$ g by about 20%. Because nonmetallic projectiles are difficult to accelerate, we have no results for glass projectiles impacting at $\alpha = 60°$. Polyphenylene projectiles which impacted on the film at an angle $\alpha = 60°$ could no longer be detected behind the film. This implies that these projectiles are decelerated below 1 km/sec or even completely stopped by the film.

3. DETERMINATION OF THE PENETRATION LIMIT OF THE HELIOS FILM

An important parameter studied in the simulation experiments was the plasma pulse registered behind the film (third time mark, Fig. 1). Only the results of iron projectiles (high density) and of polyphenylene projectiles (low density) are shown in Fig. 3. Aluminium and glass gave intermediate results. Figure 3 illustrates a comparison of the results of the plasma measurements after the film penetration (lower panel of Fig. 3) with the corresponding calibration, at which the film was replaced by a grid (upper panel). The plasma pulse Q is normalised to the projectile mass m because it had been shown that $Q \sim m$ at $v = \text{const.}$ (Dietzel *et al.* 1973). In the two lower diagrams of Fig. 3 the plasma pulse is plotted as a function of the original speed v_1 of the projectiles. No significant differences within the scatter of the measurement can be seen between the deceleration measurement of iron projectiles and the calibration (dashed line). This is due to the very small deceleration (<10%) of iron projectiles. This is quite different for polyphenylene projectiles, which have densities of $\rho = 1.25\ \text{g/cm}^3$. Such projectiles impacting at angles $\alpha = 0°$ and $\alpha = 30°$ show an attenuation of the plasma pulse by about a factor of 10. Polyphenylene projectiles which impact at an angle of incidence of $\alpha = 60°$ could not be detected. In order to study the fragmentation upon penetration, iron projectiles with $m = 10^{-12}$–10^{-13} g and $v = 7$–8 km/sec were shot onto a gold target with an angle of incidence $\alpha = 30°$. A typical impact crater can be seen by the scanning electron microscope (SEM) photograph in Fig. 4 (upper part). If the Helios film is mounted directly in front of the gold target, the projectile shows the typical impact pattern as illustrated in Fig. 4 (lower part). The projectile bursts into many

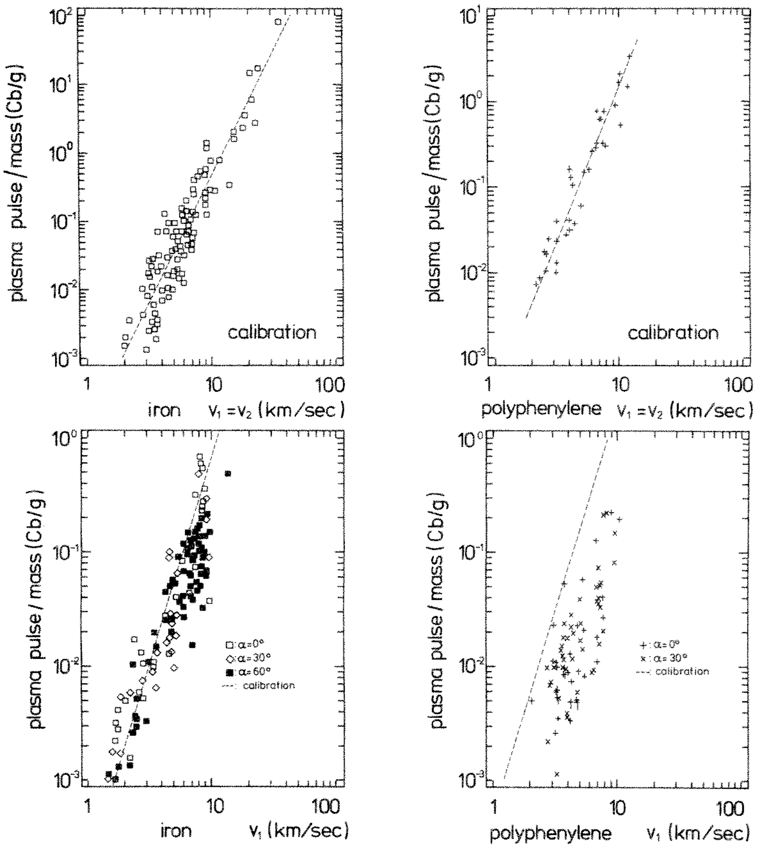

FIG 3. THE PLASMA PULSE NORMALISED TO THE MASS IS PLOTTED VERSUS v_1.
Upper panel: calibration (without film in front of the plasma detector). Lower panel: measurement (with film in front of the plasma detector).

Erratum

THE PENETRATION LIMIT OF THIN FILMS

N. Pailer and E. Grün

p 325 Fig. 4 Iron projectiles of the same mass and speed hitting a gold target at angle of incidence $\alpha = 30^\circ$. Lower part: direct impact. Upper part: impact after penetration of the Helios film.

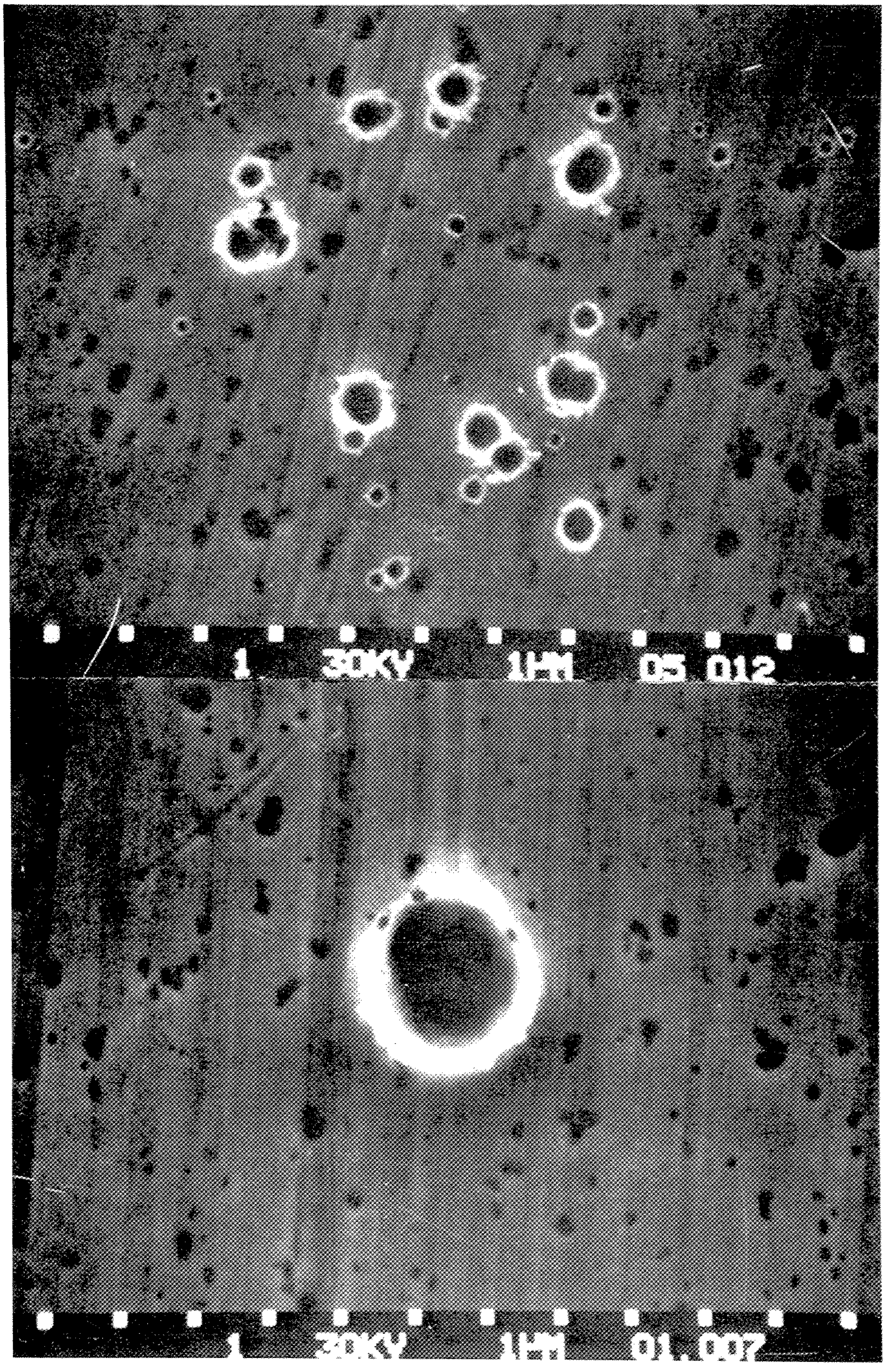

FIG 4. IRON PROJECTILES OF THE SAME MASS AND SPEED HITTING A GOLD TARGET AT ANGLE OF INCIDENCE $\alpha = 30°$.

Upper part: direct impact. Lower part: impact after penetration of the Helios film.

-4- B33271-000A

Planet. Space Sci., Vol. 28, pp. 333–349. Pergamon Press Ltd., 1980. Printed in Northern Ireland

74-097A-12A
DSC # 514

ORBITAL AND PHYSICAL CHARACTERISTICS OF MICROMETEOROIDS IN THE INNER SOLAR SYSTEM AS OBSERVED BY *HELIOS 1*

E. GRÜN, N. PAILER, H. FECHTIG and J. KISSEL
Max-Planck-Institut für Kernphysik, Postfach 10 39 80, 6900 Heidelberg

(*Received* 6 *August* 1979)

Abstract—The *Helios 1* spacecraft was launched in December 1974 into a heliocentric orbit of 0.3 *AU* perihelion distance. *Helios 2* followed one year later on a similar orbit. Both spaceprobes carry on board micrometeoroid experiments each of which contains two sensors with a total sensitive area of 121 cm^2. To date, only preliminary data are available from *Helios 2*. Therefore the results presented here mainly apply to data from *Helios 1*. The ecliptic sensor of *Helios 1* measures dust particles which have trajectories with elevations from $-45°$ to $+55°$ with respect to the ecliptic plane. The south sensor detects dust particles with trajectory elevations from $-90°$ (ecliptic south-pole) to $-4°$. The ecliptic sensor is covered by a thin film (3000 Å parylene coated with 750 Å aluminium) as protection against solar radiation. The other sensor is shielded by the spacecraft rim from direct sunlight and has an open aperture. Micrometeoroids are detected by the electric charge produced upon impact. During the first 6 orbits of *Helios 1* around the sun the experiment registered a total of 168 meteoroids, 52 particles were detected by the ecliptic sensor and 116 particles by the south sensor. This excess of impacts on the south sensor with regard to the impacts on the ecliptic sensor is due predominantly to small impacts which are characterized by small pulse heights of the charge signals. But also large impacts were statistically significantly more abundant on the south sensor than on the ecliptic sensor. Most impacts on the ecliptic sensor were observed when it was pointing in the direction of motion of Helios (apex direction). In contrast to that the south sensor detected most impacts when it was facing in between the solar and antapex direction. Orbit analysis showed that the "apex" particles which are predominantly detected by the ecliptic sensor have eccentricities $e < 0.4$ or semi-major axes $a \leq 0.5$ *AU*. From a comparison with corresponding data from the south sensor it is concluded that the average inclination $\bar{i}$ of "apex" particles is $\bar{i} < 30°$. The excess of impacts on the south sensor, called "eccentric"particles, have orbit eccentricities $e > 0.4$ and semimajor axes $a > 0.5$ *AU*. β-meteoroids leaving the solar system on hyperbolic orbits are directly identified by the observed imbalance of outgoing (away from the sun) and ingoing particles. It is shown that "eccentric" particles, due to their orbital characteristics, should be observable also by the ecliptic sensor. Since they have not been detected by this sensor it is concluded that the only instrumental difference between both sensors, i.e. the entrance film in front of the ecliptic sensor, prevented them from entering it. A comparison with penetration studies proved that particles which do not penetrate the entrance film must have bulk densities ρ(g/cm^3) below an upper density limit $\rho_{\max}$. It is shown that approximately 30% of the "eccentric" particles have densities below $\rho_{\max} = 1$ g/cm^3.

1. INTRODUCTION

On December 10, 1974 *Helios 1* was launched into an elliptic orbit around the sun with a perihelion distance of 0.31 *AU*. A second spacecraft (*Helios 2*) followed on January 15, 1976 on a similar orbit with a perihelion distance of 0.29 *AU*. The orbit of *Helios 1* and *Helios 2*, respectively, has a semi-major axis of 0.65 *AU* (0.64 *AU*) and an eccentricity of 0.52 (0.54). The inclinations of both orbits are about 0°. Both spaceprobes carry almost identical instrumentation. These missions provided the first opportunity to investigate interplanetary dust inside the orbits of Venus and even Mercury. Both zodiacal light observations (Leinert *et al.* 1977 and 1979) and *in-situ* measurements of micrometeoroids (Grün *et al.* 1977) are performed on board of both spacecrafts. The only other space-probe carrying a micrometeoroid experiment inside the Earth's orbit, which yielded significant results (Rhee *et al.* 1974) was *Pioneer 9* with a perihelion distance of 0.76 *AU*.

The study of interplanetary dust in the inner solar system is of great importance because most phenomena related with interplanetary dust are enhanced close to the sun. The Poynting Robertson effect causes the dust particles to spiral towards the sun which gives rise to an increased spatial density of dust close to the sun (Briggs, 1962). Due to a higher spatial density the micrometeoroids collide more frequently with each other (Zook and Berg, 1975, Dohnanyi, 1976) and thus diminish the number of big particles while producing large numbers of smaller particles by impact fragmentation. Parts of these fragments have been observed even at 1 *AU* as meteoroids on high elliptical orbits (Grün and Zook, 1980), being detected by satellite detectors from their apex direction (Berg and Gerloff, 1971, Hoffmann *et al.* 1975b) or as β-meteoroids (Berg and Grün, 1973) leaving the solar system on hyperbolic orbits under the prevailing action of radiation pressure. Comets inject high amounts of dust in the vicinity of the sun (Whipple, 1955) most of which, of course, will leave the inner solar system as fast as the comet does (Röser, 1976). Theoretical studies of the interaction of dust particles with the interplanetary plasma and magnetic field (Morfill and Grün, 1979 a, b) suggest that the orbits of micrometeoroids are systematically altered by this interaction with high efficiency close to the sun. All these effects may be more easily studied at 0.3 *AU* from the sun than at the earth's orbit.

The objective of the micrometeoroid experiments on the Helios mission is to investigate the distribution of interplanetary dust in the inner solar system, to study its dynamics and to determine the physical and chemical characteristics of micrometeoroids. The spatial density distribution is best obtained by zodiacal light observations (Link *et al.* 1976, Leinert *et al.* 1979) which determine the integrated effect of a very large number of particles. Link *et al.* (1976) reported an increase of the spatial density n with decreasing solar distance r as $n \propto r^{-1.3}$. The *in-situ* experiment which measures individual dust particles impacting on the sensor always struggles with large statistical uncertainties because of the small number (order of 100) of observed micrometeoroids (Grün *et al.* 1977). On the other hand an *in-situ* experiment yields information on the dynamical state and the physical and chemical characteristics of particles.

This paper describes results obtained from the analysis of the dynamical and physical parameters observed by the micrometeoroid experiments on the Helios mission. Only directly measured parameters like sensor azimuth and spacecraft position at the time of impact and total charge released upon impact will be used in this analysis in order to avoid uncertainties introduced by applying empirical calibrations First results from an orbit analysis of the observed particles have been reported by Schmidt and Grün (1978). Analysis of the chemical data received by the Helios micrometeoroid experiments is forthcoming.

2. INSTRUMENTATION

The micrometeoroid experiment on board the Helios spacecraft consists of two individual sensor units and a common electronic data processor. Figure 1 shows a schematic cross section of *Helios 1* with the mounting positions of the two sensors. The spin axis of the Helios spaceprobe is perpendicular to its orbital plane which is also the ecliptic plane. While the spacecraft spins around its axis within a period of 1 sec the two sensors scan a full circle in azimuth. Two sensors are installed in order to allow a rough determination (two channels) of the ecliptic elevation of a particle's trajectory. The antenna of *Helios 1* is pointing to the ecliptic north pole, whereas the *Helios 2* spacecraft is turned over and its antenna is pointing to the ecliptic south pole.

The axis of the ecliptic sensor (of both *Helios 1* and *2)* forms an angle of 65° with the positive spin axis of the spacecraft which is the direction the antenna is pointing. Because this sensor is viewing the sun once per revolution, it is covered by a thin

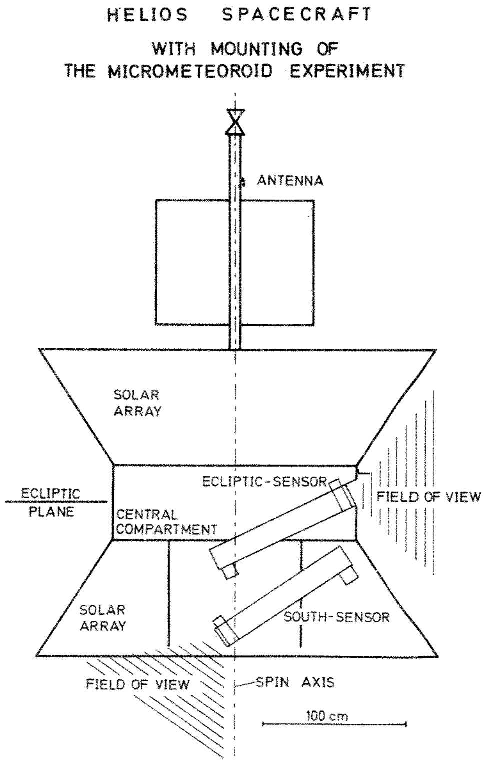

FIG. 1. SCHEMATIC VIEW OF THE *Helios 1* SPACECRAFT WITH MOUNTING POSITIONS OF THE DUAL SENSOR MICROMETEOROID EXPERIMENT.

The antenna of *Helios 1* points towards the ecliptic north pole whereas that of *Helios 2* points towards the ecliptic south pole.

Erratum

ORBITAL AND PHYSICAL CHARACTERISICS OF MICROMETEOROIDS IN THE INNER SOLAR SYSTEM AS OBSERVED BY HELIOS 1

E. Grün, N. Pailer, H. Fechtig and J. Kissel

p 335 Table 1 (a). Ecliptic Sensor
Table 1 (b). South Sensor

p 338 particle velocity vector $\underline{v}$
Helios velocity vector $\underline{v}'$
relative velocity vector $\underline{u} = \underline{v} - \underline{v}'$

film (3000 Å parylene coated with 750 Å aluminium) as protection against direct solar radiation and solar wind particles. The axis of the south sensor (*Helios 1)* and the north sensor (*Helios 2),* respectively, form an angle of 134° with the positive spin axis. Since this sensor is not exposed to direct sun light its aperture is open. It has just a grid system for solar wind protection in front of the sensitive area. The field of view of each sensor is a cone with half angle 65° (ecliptic sensor) and 73° (south sensor), respectively, centered on the sensor axis. In elevation the fields of view are limited by the spacecraft rim (south sensor) and by an external blind (ecliptic sensor). Table 1 gives the relative angular sensitivity $f(\vartheta, \varphi)$ as a function of the polar coordinates ($\vartheta = 0°$ being the sensor axis) for both sensors. The relative angular sensitivity is defined as the sensitive area $F(\vartheta, \varphi)$ projected in the direction given by the angles ϑ and φ normalised to $F_o = F(0°, \varphi)$:

$$f(\vartheta, \varphi) = F(\vartheta, \varphi)/F_o \qquad (1)$$

The values of F_o for the sensors are: ecliptic sensors $F_o = 54.5\ \text{cm}^2$, south/north sensors $F_o = 66.5\ \text{cm}^2$ where the special aperture geometries and the transmission of the grids which are in front of the sensitive target areas have been taken into account. The different apertures of the sensors influence the width and the shape of the fields of view. Also the different configurations of the blinds can be seen in the data ($\varphi = 0°$). At $\varphi = 270°$ and $\vartheta > 30°$ an external structure is obscuring the field of view of the south (north) sensor. The effective solid angle Ω for each sensor is obtained from

$$\Omega = \int_{0°}^{90°} \int_{0°}^{360°} f(\vartheta, \varphi) \sin \vartheta \, d\varphi \, d\vartheta \qquad (2)$$

Numerical integration yields $\Omega = 1.04$ sterad for the ecliptic sensors and $\Omega = 1.39$ sterad for the south and north sensors. The sensitivity for particles hitting a sensor from a direction which has an elevation γ with respect to the ecliptic plane is shown in Fig. 2. This sensitivity has been calculated by integration of the appropriate relative angular sensitivity over a full spin revolution. It can be seen that the south sensor and the ecliptic sensor of *Helios 1* detect particles from $-90° < \gamma < -4°$ and $-45° < \gamma < +55°$, respectively. These numbers have to be inverted for *Helios 2.*

TABLE 1. ANGULAR SENSITIVITY OF BOTH HELIOS SENSORS AS A FUNCTION OF THE POLAR COORDINATES ϑ AND φ.

The sensor axis is defined by $\vartheta = 0°$. An external blind (ecliptic sensor) and the spacecraft rim (south sensor) cut into the field of view at $\varphi = 0°$.

φ \ ϑ	0°	10°	20°	30°	40°	50°	60°	70°	80°	90°
0°	1.00	0.75	0.33	0.01	0.00	0.00	0.00	0.00	0.00	0.00
30°	1.00	0.78	0.42	0.08	0.00	0.00	0.00	0.00	0.00	0.00
60°	1.00	0.87	0.64	0.38	0.14	0.00	0.00	0.00	0.00	0.00
90°	1.00	0.92	0.79	0.63	0.43	0.23	0.06	0.00	0.00	0.00
120°	1.00	0.95	0.82	0.65	0.44	0.24	0.06	0.00	0.00	0.00
150°	1.00	0.97	0.84	0.65	0.44	0.24	0.06	0.00	0.00	0.00
180°	1.00	0.97	0.85	0.66	0.45	0.24	0.06	0.00	0.00	0.00
210°	1.00	0.97	0.84	0.65	0.44	0.24	0.06	0.00	0.00	0.00
240°	1.00	0.95	0.82	0.65	0.44	0.24	0.06	0.00	0.00	0.00
270°	1.00	0.92	0.79	0.63	0.43	0.23	0.06	0.00	0.00	0.00
300°	1.00	0.87	0.64	0.38	0.14	0.00	0.00	0.00	0.00	0.00
330°	1.00	0.78	0.42	0.08	0.00	0.00	0.00	0.00	0.00	0.00

TABLE 1(a). SOUTH SENSOR

φ \ ϑ	0°	10°	20°	30°	40°	50°	60°	70°	80°	90°
0°	1.00	0.95	0.74	0.00	0.00	0.00	0.00	0.00	0.00	0.00
30°	1.00	0.95	0.83	0.24	0.00	0.00	0.00	0.00	0.00	0.00
60°	1.00	0.95	0.87	0.72	0.30	0.00	0.00	0.00	0.00	0.00
90°	1.00	0.95	0.87	0.73	0.55	0.35	0.17	0.02	0.00	0.00
120°	1.00	0.95	0.87	0.73	0.55	0.35	0.17	0.02	0.00	0.00
150°	1.00	0.95	0.87	0.73	0.55	0.35	0.17	0.02	0.00	0.00
180°	1.00	0.95	0.87	0.73	0.55	0.35	0.17	0.02	0.00	0.00
210°	1.00	0.95	0.87	0.73	0.55	0.35	0.17	0.02	0.00	0.00
240°	1.00	0.95	0.87	0.73	0.55	0.35	0.16	0.02	0.00	0.00
270°	1.00	0.95	0.87	0.73	0.53	0.25	0.05	0.00	0.00	0.00
300°	1.00	0.95	0.87	0.72	0.28	0.00	0.00	0.00	0.00	0.00
330°	1.00	0.95	0.85	0.22	0.00	0.00	0.00	0.00	0.00	0.00

TABLE. 1(b). ECLIPTIC SENSOR

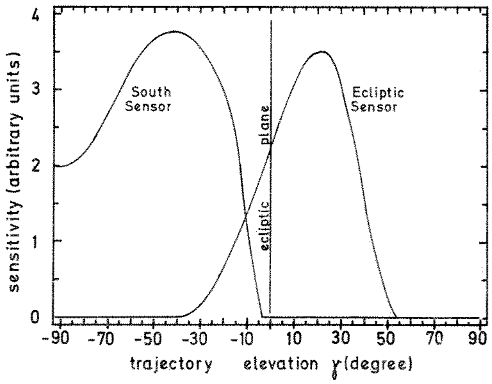

FIG. 2. SENSITIVITY OF THE *Helios 1* SENSORS WITH REGARD TO PARTICLES HITTING THE SENSORS FROM A DIRECTION WHICH HAS THE ELEVATION γ WITH RESPECT TO THE ECLIPTIC PLANE.

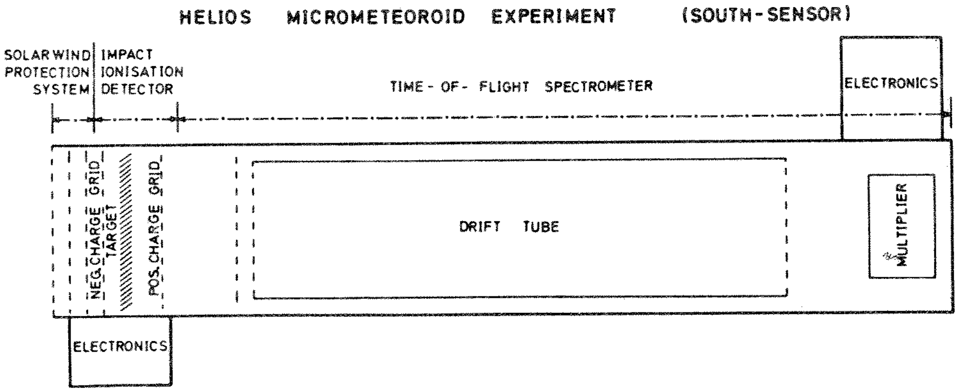

FIG. 3. CROSS-SECTION OF THE SOUTH (NORTH) SENSOR.
Micrometeoroids hit the venetian blind type target after passing a grid system for solar wind protection. Impact charges are detected by grids in front of (negative charge) and behind (positive charge) the target. A time-of-flight mass spectrum of the ions released upon impact is measured by a particle multiplier at the end of a 80 cm-drift tube.

The cross-section of the south (north) sensor is shown in Fig. 3. The sensor consists of the solar wind protection system, the impact ionisation detector and the time-of-flight spectrometer. Two small electronic boxes containing preamplifiers and high voltage power supplies are directly attached to the sensor. Five quantities are generally measured if a micrometeoroid hits the venetian blind type target with an impact speed in excess of approximately 1 km/sec: (1) the total negative charge (electrons) and (2) the total positive charge (ions) released upon the impact, (3) the rise-time of the negative charge pulse, (4) the rise-time of the positive charge pulse and (5) the time-of-flight spectrum of the ions. The instrument is triggered when a signal exceeds the threshold of either the positive or negative charge channel. With the south or north sensor additionally the electrostatic charge (6) of the dust particles is measured by the charge induced on a grid in front of the target. With the ecliptic sensor the flight-time (7) of the dust particle is measured between the penetration of the entrance film and the impact on the target. The *Helios 1* experiment has a sensitivity threshold for micrometeoroids with masses of approximately 3×10^{-13} g at an impact speed of 10 km/sec. The measured parameters allow the determination of the particle mass, speed, electrostatic charge and composition of the plasma produced by the impact onto the sensor. Further details of the impact plasma detector are given by Dietzel *et al.* (1973) and Grün *et al.* (1979).

Besides the parameters measured directly from the impact, additional information is gathered and transmitted to earth: (8) various coincidences between the measured signals, enabling one to discriminate between noise and "probable" impacts, (9) the time at which the event has occurred, and (10) the pointing direction (azimuth) of the sensor. If a "probable" impact is indicated by proper coincidences, the count in one out of four registers is increased by one, this register is selected according to the amplitude of the positive charge signal (ion amplitude: IA). By this method one obtains from the four counters the number of "probable" impacts within 4 positive-charge-intervals roughly corresponding to 4 different mass intervals of micrometeoroids.

All the information on one event is contained in an experiment-data-frame of 256 bits, 180 of which comprise the time-of-flight spectrum of the impact plasma. There exist 4 buffers in the experiment. Each contains a complete experiment-data-frame. The buffer is also selected according to the amplitude of the positive charge signal (IA). Because noise occurs most frequently with low signal amplitudes the buffer corresponding to the smallest charge signals ($IA \leq 4$) has the highest noise rate. Since any event (impact or noise) introduces a dead-time the data from impacts with small positive charges $IA \leq 4$ are less complete than the large impact events. These four different experiment-data-frames are successively transmitted to earth with a rate of one per 20 s to 20 min (depending on the Helios–earth distance).

The sensitivity of the *Helios 2* sensors has been electronically increased by a factor of 2.5. Because of an unexpected high noise background on board the *Helios 2* spacecraft in combination with the increased sensitivity of the experiment the total dead-time has been increased considerably and consequently the number of observed impacts is lower when compared with *Helios 1*. A full analysis of the data from *Helios 2* requires further work. Therefore in this paper only data from *Helios 1* are presented although the main effects observed in the *Helios 1* data are seen in the *Helios 2* data, too.

The results presented in this paper are based on data from the first 6 revolutions of *Helios 1* around the sun, from 12 December 1974 to 26 January 1978. During a total time of 53 days the experiment on board *Helios 1* was not active. The remaining 1089 days the experiment was active and transmitted data back to Earth. Gaps in the data transmission (when the data could not be received on ground) were partly covered by an on board memory of 0.5 megabit capacity, which was readout after the gaps. Both helios spacecrafts and the experiments are still operating and continue to transmit data back to Earth.

3. DETECTION PROBABILITY OF ELLIPTIC METEOROID ORBITS

The orbit of the Helios spacecraft and the sensor characteristics determine the selection of meteoroid orbits which can be observed by the experiment, e.g. only micrometeoroids can be observed which have their aphelia outside 0.3 AU and their perihelia inside 1.0 AU, The south sensor detects only particles in their ascending nodes, i.e. when they cross the ecliptic plane from the south to the north of the ecliptic plane. In the following the probability of detecting particles due to this selection effects will be discussed for both sensors of *Helios 1*. This analysis also applies to *Helios 2* accordingly. Schmidt (1977) discussed some general selection effects which predominantly have significance on hyperbolic orbits, while here the analysis is restricted to bound orbits around the sun.

For this analysis only gravitation and radiation pressure is taken into account, other effects like electromagnetic interactions are neglected because they are assumed to be of minor direct significance for the particles trajectories within the accuracies involved. Although electromagnetic interaction may be of great importance for the secular evolution of dust orbits (Morfill and Grün, 1979a) its effect on the overall orbit distribution may be difficult to determine in an individual meteoroid trajectory by an *in situ* impact detector.

An orbit of a dust particle is characterised by its semimajor axis a, its eccentricity e and inclination i (for convenience the reciprocal value $1/a$ is taken). In addition, the effect of radiation pressure on the particle has to be taken into account. The radiation pressure constant β is the ratio of the force of radiation pressure F_{rad} over that of gravity F_{grav}

$$\beta = F_{\text{rad}}/F_{\text{grav}}. \tag{3}$$

This radiation pressure constant depends on the size of the particle, its density and the optical characteristics of its material (e.g. Schwehm and Rhode, 1977). For big particles (i.e. larger than 10 μm radius) the radiation pressure constant is $\beta \leqslant 0.01$ for most materials, while micron-sized and smaller particles may have values of $\beta \geqslant 0.5$ and for some materials (e.g. metals) β is even exceeding 1. For submicron-sized dielectric particles β is decreasing again. But for these particles ($m \leqslant 10^{-14}$g) electromagnetic interactions become increasingly important (Morfill and Grün, 1979a, b) and their orbits can no longer be treated as Kepplerian orbits. Since values of $\beta > 0.5$ generally lead to hyperbolic orbits (Zook and Berg, 1975) we only consider values of $\beta < 0.5$ for our analysis of bound orbits. Further assumptions of the following analysis are: 1) the longitude of the ascending node Ω, and 2) the argument of perihelion ω are uniformly distributed over $[0, 2\pi]$, and 3) retrograde orbits, i.e. inclination $i > 90°$, have not been taken into account for the following reasons. Although the observable flux of particles on retrograde orbits is higher for a given spatial density than that of particles on prograde orbits, due to the higher relative speed between an observer and the meteoroids, Southworth and Sekanina (1973), and Sekanina and Southworth (1975) report that only approximately 1% of all their observed meteorparticles are on retrograde orbits. Also Hoffmann *et al.* (1975b) report from HEOS-2 measurements that particles with masses $m > 10^{-13}$g have impact speeds $v \leqslant 23$ km/sec which is not compatible with retrograde orbits.

It has been further assumed that the field of view in elevation with respect to the ecliptic plane extends, with equal sensitivity, for the south sensor from −90° to −10° and for the ecliptic sensor from −10° to +40°. These ranges correspond roughly to the ranges of maximum elevation sensitivity of both sensors given in Fig. 2. In this analysis the relative velocity vector between Helios and the dust particle has been calculated. Then the elevation of the particle's trajectory is evaluated: whether it is in the field of view of the sensor or not. For a given set of particle parameters ($1/a$, e, i and β) the heliocentric velocity of the particle $\mathbf{v}$ and that of

Helios $\mathbf{v}$ at the distance r between Helios and the sun has been calculated. In a rectangular coordinate system with v_x in radial direction, v_y being perpendicular to v_x in the ecliptic plane and v_z perpendicular to the ecliptic plane, the components of the velocity are given by:

$$v_x^2 = \mu(1-\beta)\left(\frac{2}{r}-\frac{1}{a}-\frac{a}{r^2}(1-e^2)\right) \qquad (4)$$

$$v_y^2 = \mu(1-\beta)\frac{a}{r^2}(1-e^2)\cos^2 i \qquad (5)$$

$$v_z^2 = \mu(1-\beta)\frac{a}{r^2}(1-e^2)\sin^2 i \qquad (6)$$

with $\mu = GM = 1.33\times10^{26}\ \mathrm{cm}^3\ \mathrm{sec}^{-2}$ (G = gravitational constant, M = solar mass). The velocity components of Helios are obtained by substituting the corresponding parameters of Helios: $a = 9.7\times10^{12}$ cm, $e = 0.52$, $i = 0°$ and $\beta = 0$. In order to calculate the relative velocity vector $\mathbf{V} = \mathbf{v} - \mathbf{u}$ we have to realize that 8 different combinations of the speed components are possible, at a given distance r from the sun, not considering retrograde orbits: $u_x = \pm v_x \mp v_x'$ corresponding to inbound/outbound trajectories of the particle and Helios, $u_y = v_y - v_y'$ and $u_z = \pm v_z$ corresponding to ascending/descending node of the particle orbit. The elevation γ of this trajectory with respect to Helios is given by

$$\tan\gamma = u_z(u_x^2 + u_y^2)^{-1/2} \qquad (7)$$

For a given set of parameters ($1/a$, e, i, β and r) we have determined whether this particle trajectory is within the field of view of a sensor or not. Figures 4 and 5 show the result of this analysis for the ecliptic sensor and the south sensor. For fixed values of β and i the parameters $1/a$, e and r have been varied in small steps. In the $1/a$ *vs* e plane the relative number of orbits observable by one sensor is given. Due to the variation of r up to 70 different trajectories with given $1/a$ and e values have been calculated. The chequered areas show that all trajectories with the corresponding $1/a$ and e values are observable (probability = 1), blank areas correspond to non observable orbits. The ecliptic sensor has the highest probability of observing meteoroids with high eccentricities and low semimajor axes ($1/a$ large). These orbits are seen both in their ascending and descending node. The south sensor only observes orbits in their ascending node and therefore maximum probability is only 0.5. It is biased towards orbits with small eccentricities. Since a variation of the radiation pressure constant β from 0 to 0.4 does not affect the visibility of orbits too strongly, only results for $\beta = 0.2$ are given. This corresponds e.g. to an olivine particle with 1 μm radius (Schwehm and Rhode, 1977). Orbits with $\beta = 0.4$ are slightly better observable by the ecliptic sensor than those with $\beta = 0$, due to the somewhat higher relative speed which tends to concentrate the trajectories towards the ecliptic plane. On the other hand, the south sensor observes big particles ($\beta = 0$) slightly better. The inclinations of

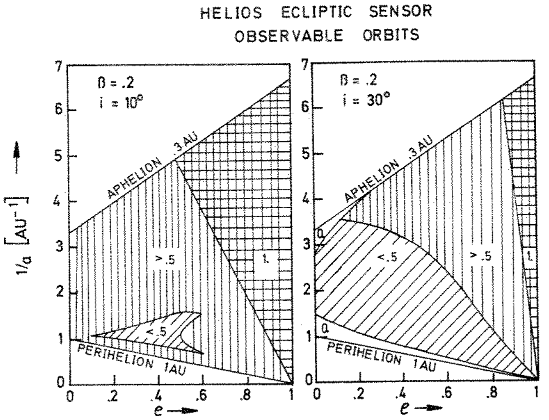

FIG. 4. DETECTION PROBABILITY OF MICROMETEOROID ORBITS BY THE ECLIPTIC SENSOR.

The radiation pressure constant β of the particles has been assumed $\beta = 0.2$ and the inclination i of the orbits is varied. Blank areas correspond to non observable orbits. Only orbits with aphelia outside 0.3 *AU* and perihelia inside 1.0 *AU* are observable. The chequered areas indicate that all particles with the corresponding orbital elements a and e which hit the Helios spaceprobe are observable by that sensor. Striped areas correspond to intermediate detection probabilities.

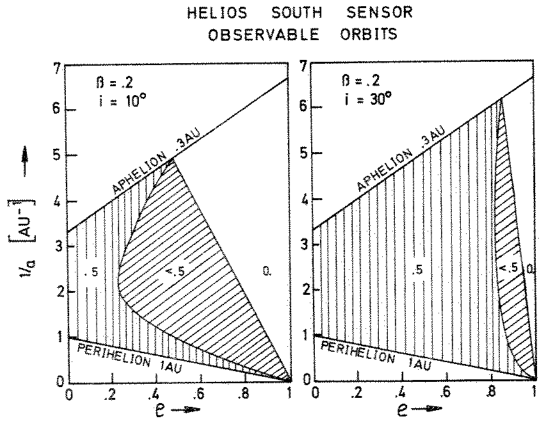

FIG. 5. DETECTION PROBABILITY OF MICROMETEOROID ORBITS BY THE SOUTH SENSOR.

For further description, see Fig. 4.

Erratum

ORBITAL AND PHYSICAL CHARACTERISICS OF MICROMETEOROIDS IN THE INNER SOLAR SYSTEM AS OBSERVED BY HELIOS 1

E. Grün, N. Pailer, H. Fechtig and J. Kissel

p 335 Table 1 (a). Ecliptic Sensor
Table 1 (b). South Sensor

p 338 particle velocity vector $\underline{v}$
Helios velocity vector $\underline{v}'$
relative velocity vector $\underline{u} = \underline{v} - \underline{v}'$

account the different impact speeds of the particles onto the sensors, which results in different sensitivity thresholds. In that range of the $1/a$–e–plane, where both sensors can observe dust orbits, there are no systematic differences of the impact speeds on both sensors. Those orbits which are observable by the ecliptic sensor alone, i.e. high eccentricities and small semimajor axes, have impact speeds in the range from approx. 30 to 70 km/sec. The orbits which can be observed by the south sensor alone, i.e. small eccentricities and perihelia close to 1 AU and aphelia close to 0.3 AU have impact speeds from approx. 10 to 40 km/sec. This systematic difference in the impact speed corresponds to a higher sensitivity of the ecliptic sensor, i.e. this sensor can observe the more abundant smaller particles.

The distribution of orbital elements of meteor particles by Sekanina and Southworth (1975) shows an increased density towards large semimajor axes and a peak density between eccentricities $e = 0.2$ and $e = 0.7$. According to these authors half of the meteoroid orbits have inclinations $i < 20°$ while the other half have inclinations $i > 20°$. This orbit distribution is similar to the one used by Singer and Bandermann (1967) in order to describe zodiacal light observations; their orbit distribution had an average orbit inclination of approximately $\bar{i} = 30°$.

Taking into account the different selection effects for the particle orbits observable by both Helios

$$Q = cmv^{\eta} \tag{9}$$

$$\left.\begin{aligned}\eta &= 2.75\\ c &= 3.3 \times 10^{-5}\end{aligned}\right\}\text{for positive charges}$$

$$\left.\begin{aligned}\eta &= 4.4\\ c &= 7.8 \times 10^{-6}\end{aligned}\right\}\text{for negative charges.}$$

The difference of the speed dependence of the charge signals of different polarities comes from the variation of the energy distributions of ions and electrons and the correspondingly varying collection efficiency of the detector system. Generally the collection efficiency for the ions is smaller than that for the electrons and is further decreased with increasing speed.

In this section the pulse height distribution of the positive charge signals (IA) which are released upon impacts of micrometeoroids onto the Helios sensors is discussed. This pulse height is measured in a dynamic range of 10^4, the corresponding charge ranges from 5×10^{-15} to 5×10^{-11} C. This dynamic range is divided into 16 steps ($IA = 0$–$IA = 15$) which are separated by a constant factor of approx. 1.8. If the charge signal exceeds the measurement range an overflow (OF) is indicated in the data.

An impact of a dust particle is identified if several signals measured from this event are coincident within a narrow time-interval. These coincidence requirements were established and verified during the calibration of the instrument. The most affirmative coincidences are the occurrence of both the positive and negative charge signals within a 12 μsec time-interval and the subsequent measurement of a time-of-flight spectrum of the ions released upon impact within approx. 50 μsec. By the first criterion the simultaneous occurrence of both the electron and ion charge signal some 240 "probable" impact events were found in the data during the first six orbits of *Helios 1* around the sun (12 December 1974–26 January 1978). None of these "probable" impact events occurred during times of increased solar cosmic ray activities or interplanetary shock events.

One hundred and sixty-eight of the "probable" events had measureable time-of-flight spectra and were identified as "true" impact events, only these are considered in the following analysis. Figure 6 shows the orbits of the Earth and *Helios 1*. The heavy dots superimposed onto the Helios orbit mark the places where micrometeoroid impacts were observed and the direction of the bars attached to these points represent the sensor pointing direction at the time of impact. Since the sensors have wide fields of view, the true impact direction may deviate from the direction shown by up to 60° or 70°. The length of the bars indicate the measured pulse height (IA) of the positive charge signal. The pulse height represented by the longest bars ($IA = 15$) is 10^4 times larger than the pulse height represented by the shortest bars ($IA = 0$).

The true number of micrometeoroid impacts onto the experiment is greater than the number of impacts detected in the data because of the incomplete data coverage and instrumental dead-time. This incompleteness is the same for both sensors because data from both sensors are processed commonly, i.e. dead-time for the south sensor is also dead-time for the ecliptic sensor. There is, of course, a difference in the data completeness depending on the pulse-height of the considered events. The most complete set of data (approx. 90% complete) exist for large impacts ($IA > 4$) while small impacts ($IA \leq 4$) are only complete to approx. 50%.

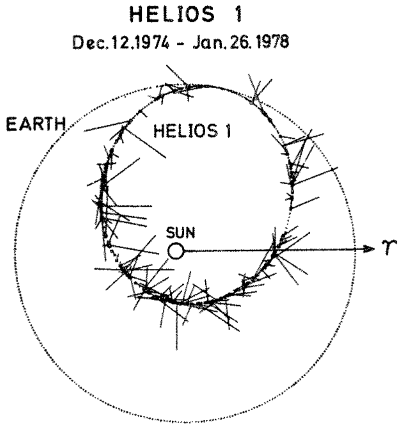

FIG. 6. IMPACTS DETECTED DURING THE FIRST 6 ORBITS OF *Helios 1* AROUND THE SUN.

Bars attached to the heavy dots indicate the pointing direction of the experiment at the time of impact. The length of the bars represent the magnitude of the charge released upon impact.

The pulse height distribution of the positive impact charge (IA) is shown in Fig. 7. Impacts onto the ecliptic sensor (Fig. 7a) are displayed separately from impacts onto the south sensor (Fig. 7b). Because of the different completeness of the data the number of impacts with pulse heights $IA \leq 4$ have to be multiplied by a factor of approx. 1.8 in order to be comparable with big impacts ($IA > 4$). Despite the large statistical uncertainties involved with the small numbers there is a significant excess in number of impacts detected by the south sensor (116 impacts) over that detected by the ecliptic sensor (52 impacts). This excess is both evident in the number of small impacts ($IA \leq 4$) and the number of big impacts ($IA > 4$). Two different explanations can be given at this stage in order to understand the observed excess of impacts onto the south sensor:

(a) The orbit distribution of dust particles detected by Helios is different from the distribution of meteor-orbits as described by Sekanina and Southworth 1975. The average inclination $\bar{i}$ must be larger than $\bar{i} = 30°$ and the average eccentricity $\bar{e}$ must be small $\bar{e} < 0.2$.

(b) An instrumental difference between both sensors causes the observed excess. The difference in sensitive areas and solid angles of both sensors can only account for a maximum excess of 60% and not for an excess of up to a factor of 2–3. The only other difference between both sensors is the entrance film which is only in front of the ecliptic sensor. Although no deceleration or cut-off effect has been observed during calibration with artificially accelerated iron particles, a careful study by Pailer and Grün (1980) shows that the size, speed and bulk density of the particle determine whether this particle can penetrate a film or not. This means especially that the big impacts (corresponding to large masses) which do not penetrate the entrance film must be due to low-density particles. Both effects will be discussed below in more detail.

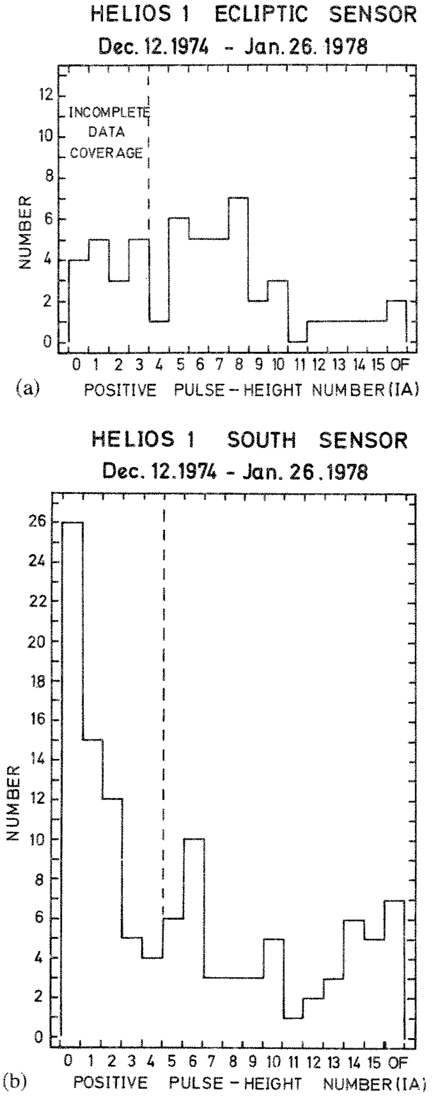

FIG. 7. PULSE HEIGHT DISTRIBUTIONS OF THE POSITIVE ION CHARGE.

The linear pulse height number (*IA*) scale corresponds to a logarithmic charge scale covering four orders of magnitude of charge.
(a) ecliptic sensor (b) south sensor

5. THE AZIMUTHAL DISTRIBUTION OF IMPACTS

During one spin revolution of the Helios spacecraft each sensor scans a full circle in azimuth. The sensor azimuth of 90° corresponds to a pointing of the sensor axis (if it is projected into the ecliptic plane) towards the sun. 0° sensor azimuth points perpendicular to the sun direction, roughly to the apex of Helios. Figure 8 shows the azimuthal distribution of impacts on both the ecliptic and the south sensor which were observed inside 0.55 *AU* from the sun. Each individual impact is represented by an area roughly corresponding to the angular sensitivity with respect to azimuth as shown in the upper right hand corner of Fig. 8a. For each sensor three curves are shown: (a) $IA \leq 2$, representing small impacts, (b) $IA > 2$ for big impacts and (c) the sum of both. The impacts detected by the ecliptic sensor show a symmetric distribution peaking at the apex direction. This type of events will be called "apex" events. Similar distributions have been observed by the cosmic dust experiments on board the

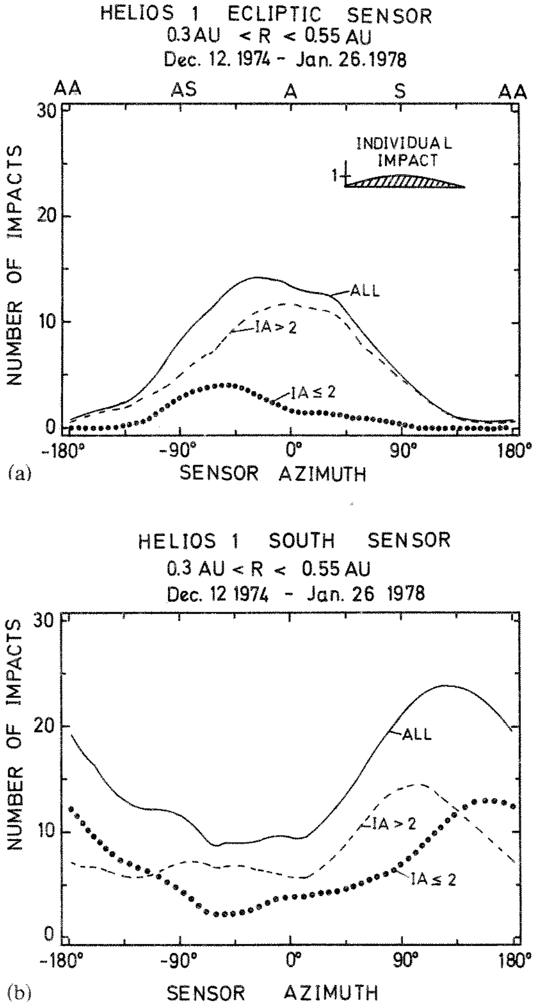

FIG. 8. AZIMUTHAL DISTRIBUTION OF IMPACTS ONTO THE HELIOS SENSORS.

An individual impact is represented by the angular probability distribution (upper right hand corner) centered on the sensor pointing direction (apex direction = 0°, sun direction = 90°)
(a) ecliptic sensor (b) south sensor

Pioneer 8 and *9* spacecrafts (Berg and Gerloff, 1971; Berg and Grün, 1973, and McDonnell, 1978) and by the dust experiment on board the HEOS-2 satellite (Hoffmann *et al.*, 1975a and b). Those impact events which were detected after the penetration of the entrance film of the *Pioneer 8/9* experiments showed this azimuthal distribution. Also the HEOS-2 experiment detected most big impacts from its apex direction. From the symmetric distribution about the apex direction it can be concluded that these particles move on bound orbits around the sun. A possible source of these "apex" dust particles is discussed by Grün and Zook (1980).

A quite different azimuthal distribution has been detected by the south sensor. Big impacts ($IA > 2$) are only half as abundant from the apex direction compared with those observed by the ecliptic sensor. This indicates that the average inclination of these "apex"-particles is $\bar{i} < 30°$. Most of the impacts were detected when the south sensor was pointing in between the solar and antapex direction. The number of impacts detected by the south sensor on the inbound leg of the Helios orbit is 59 which is almost identical with the number of impacts (57) observed during the outbound leg of the Helios orbit. Therefore the observed azimuthal asymmetry with respect to apex is true and not introduced by an imbalance of impacts along the Helios orbit. The asymmetry is best observable for small impacts $IA \leq 2$. 31 of these impacts were detected while the south sensor was pointing to the solar hemisphere (azimuth 0°–180°) compared with only 22 impacts from the anti-solar direction (azimuth −180°–0°). This finding supports the measurements from the *Pioneer 8* and *9* spaceprobes reported by Berg and Grün (1973) and McDonnell *et al.* (1975) who observed a concentration of small impacts which did not penetrate the entrance film of these experiments towards the solar direction. These "solar" particles have been discussed and interpreted by Zook and Berg (1975) and Zook (1975) to be small dust particles (β-meteoroids) leaving the solar system on hyperbolic orbits.

The difference in the data from the ecliptic sensor and the south sensor is even more clearly seen in Fig. 9a and b. Each impact is represented by its sensor azimuth and the true anomaly of Helios at the time of impact. The launch of *Helios 1* (aphelion) corresponds to a true anomaly of −180° and the perihelion corresponds to 0°. Small impacts ($IA \leq 2$) are displayed separately from big impacts ($IA > 2$). The lines shown in the graphs enclose

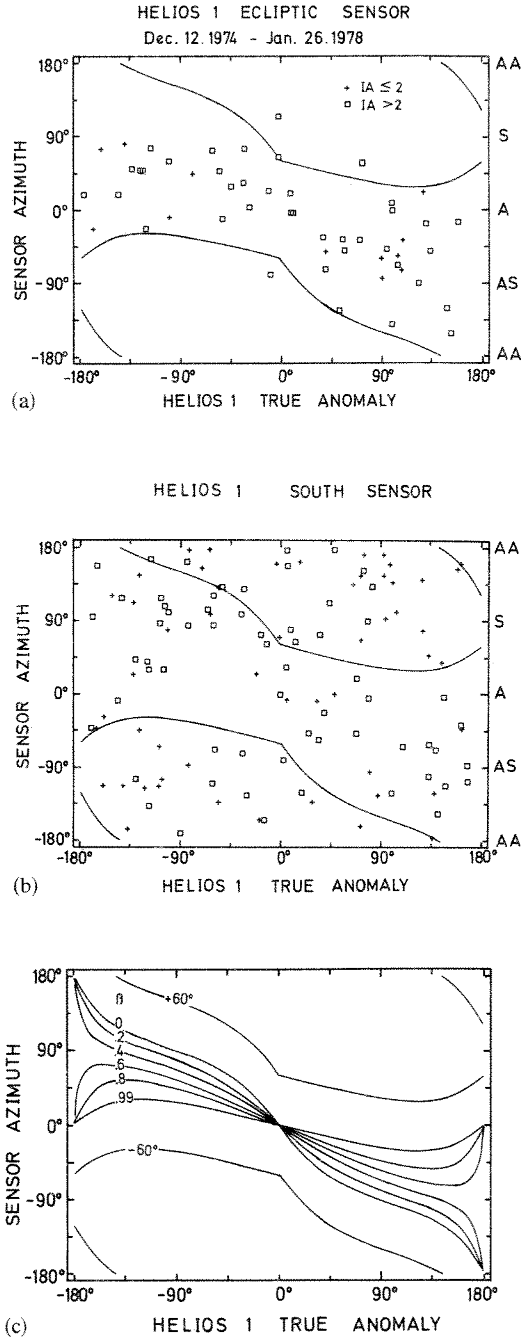

FIG. 9. SENSOR AZIMUTH *vs.* HELIOS TRUE ANOMALY FOR THE IMPACTS DETECTED BY THE HELIOS SENSORS FOR TWO PULSE HEIGHT NUMBER INTERVALS.

(a) ecliptic sensor (b) south sensor (c) sensor azimuths calculated for particles with different radiation pressure constants β on circular orbits. ±60° contours represent the limit where these particles can be observed. These lines are also shown in Fig. 9a and b.

roughly the impacts detected by the ecliptic sensor. Their significance is demonstrated in Fig. 9c: the azimuth of impacts of particles on circular orbits in the ecliptic plane have been calculated along the orbit of *Helios 1*. The position of *Helios 1* along its orbit is represented by the corresponding true anomaly. Curves are given for particles on circular orbits with different β-values, from $\beta = 0$ to $\beta = 0.99$. The so calculated band of azimuths also include inclined orbits up to an inclination of 90°. Circular orbits with an inclination of 90°, independent of the corresponding β-values, have impact azimuths which correspond to those of circular orbits in the ecliptic plane with $\beta = 0.99$. Therefore the azimuths of impact of all particles on circular orbits with inclinations from 0° to 90° lie within the band shown in Fig. 9c. Inclinations above 90° have been neglected. There are also lines shown +60° and −60° in azimuth away from the band of circular orbits. This is done in order to account for the uncertainty in the azimuth determination of impacts due to the wide field of view of the sensors. Impacts detected within this band (i.e. between the −60° and +60° line) may be due to particles on circular orbits. While impacts detected outside this band have to be due to particles on eccentric orbits (eccentricities $e > 0$), in the following these particles will be called "eccentric" particles.

The "apex" particles of the ecliptic sensor lie almost exclusively inside the ±60° band (see Fig. 9a). Only 3 out of 52 impacts were registered outside this band. This indicates that the orbital elements of the "apex" particles are confined to a range smaller than the range of all observable orbital elements. This is different for the impacts detected by the south sensor. Here the impacts are almost homogeneously scattered over the azimuth-true anomaly plane. Fifty-six of the observed impacts lie inside the ±60° band while 60 impacts were detected outside this band. The number of impacts registered by both sensors inside the band is very similar, whereas the excess of impacts detected by the south sensor are "eccentric" particles. Preliminary data from *Helios 2* support these findings: impacts on the ecliptic sensor of *Helios 2* are due to "apex" particles while impacts on the north sensor have been detected from all azimuthal directions.

6. ORBITAL CHARACTERISTICS

The Helios micrometeoroid experiment disclosed that there are, at least, 2 quite distinct groups of micrometeoroids. The first is the group of "apex" particles having been identified by the ecliptic sensor. The second group of micrometeoroids, the "eccentric" particles, have been identified by the south sensor. The different appearance of both groups in the azimuthal distribution of the impacts yields information on the orbital characteristics of the corresponding particles.

The azimuth δ of a trajectory is given by

$$\tan \delta = u_x / u_y \tag{10}$$

with u_x and u_y being the components of the relative velocity vector between the spacecraft and the dust particle in the ecliptic plane. For a given orbit of the dust particle the azimuth $|\delta|$ is largest if the spacecraft is on its inbound leg of the orbit and the particle is on its outbound leg or vice versa. If both, spacecraft and particle, are inbound or outbound the azimuth is at minimum. In addition, orbits with low inclinations, will have larger azimuths than similar orbits at high inclinations because Helios is moving in the ecliptic plane. Even for a uniform inclination distribution of dust orbits, large azimuths are biased towards low inclinations. For a given orbit (defined by a, e, i, β) only half of the possible impact configurations may give the azimuths which are required for the "eccentric" particles.

In order to get more detailed information on the orbits of the observed dust populations the azimuths of trajectories for given dust orbits have been calculated (see Fig. 10). in the $1/a$ *vs.* e plane the relative number of orbits with azimuths outside the ±60°-band as defined in Fig. 9c is given. For given $1/a$ and e values of the dust orbit the distance r, where Helios and the dust particle intersect is varied, considering 8 impact configurations: Helios inbound or outbound, dust particle inbound or outbound and dust particle at its ascending or descending node. The maximum ratio of "eccentric" orbits is 0.5, i.e. at least half of all possible trajectories and impact configurations of bound orbits have azimuths inside the ±60° band. It is shown in Fig. 10 that "eccentric" particles which can be observed by Helios have orbits with eccentricities $e > 0.4$ and $1/a < 2\,AU^{-1}$, of course, hyperbolic orbits ($e > 1$) are possible, too. Their trajectory azimuths can have any value. So far, it cannot be decided from the data presented, whether an individual particle moves on a bound or hyperbolic orbit. With increasing inclinations the number of eccentric orbits decreases and the orbits become restricted to large semimajor axes. The same effect can be seen with increasing radiation pressure constant β. All other orbits observable by

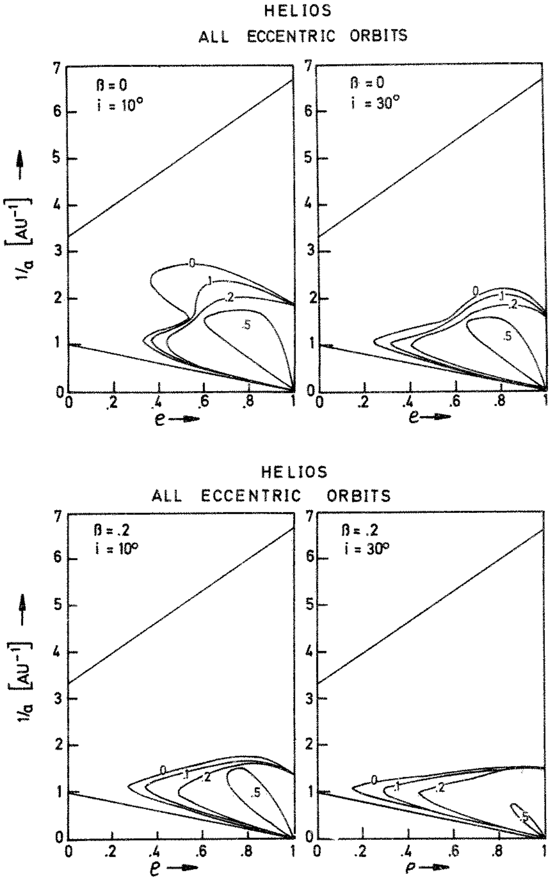

FIG. 10. "ECCENTRIC" ORBITS OBSERVABLE BY THE HELIOS SPACEPROBE.

The numbers and contours correspond to that fraction of all observable orbits which would be observed as "eccentric" particles.

Helios with aphelia outside 0.3 AU and perihelia inside 1 AU will have impact azimuths within the ±60° band.

The orbital elements of "apex" particles are restricted to small eccentricities $e < 0.4$ or small semimajor axes $a \leq 0.5\ AU$, otherwise they would show up also on eccentric orbits. Their orbits are concentrated to the ecliptic plane as has been demonstrated by the azimuthal distributions of impacts on the ecliptic and south sensor.

From the analysis of the observability of eccentric orbits follows that "eccentric" particles on bound orbits are preferentially large particles (i.e. small β!) with low orbit inclinations. Their orbits have semimajor axes larger than 0.5 AU and eccentricities in excess of 0.4 and may be even hyperbolic. Both hyperbolic β-meteoroids, leaving the solar system and particles entering the solar system are compatible with the data

More information on the nature of the "eccentric" particles can be gained from the fact that they have not been detected by the ecliptic sensor if one considers the detection probability of these particles for both sensors individually. Figure 11 shows the fraction of all observable orbits given by ($1/a$, e, i and β) that is seen by the ecliptic sensor as "eccentric" orbits. Figure 12 shows the corresponding fraction for the south sensor. The eccentric orbits of individual sensors are a subset of all eccentric orbits shown in Fig. 10. As can be seen from Figs 11 and 12 only at high inclinations ($i > 20°$) the south sensor can detect more "eccentric" particles than the ecliptic sensor. But still at $i = 30°$ almost all of the eccentric orbits observable by the south sensor are also observable by the ecliptic sensor somewhere along the Helios orbit (compare with Fig. 4), except very few orbits which have their perihelia close to 1 AU. With increasing radiation pressure constant the results do not change significantly. Since most of the "eccentric" particles have been observed by the south sensor well inside 1 AU where all orbits are also observable by the ecliptic sensor, even at high inclinations, it has to be concluded that the fact that "eccentric" particles are only detected by the south sensor is the result of an instrumental effect instead of the result of a specific orbit distribution. If the average inclination of "eccentric" particles does not exceed $\bar{i} = 30°$ both sensors are about equal sensitive for these particles.

The cut-off introduced by the entrance film of the ecliptic sensor separates the "apex" from the

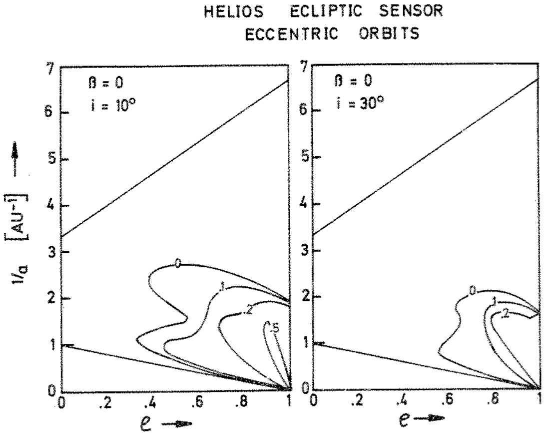

FIG. 11. OBSERVATION PROBABILITY OF "ECCENTRIC" PARTICLES BY THE ECLIPTIC SENSOR.

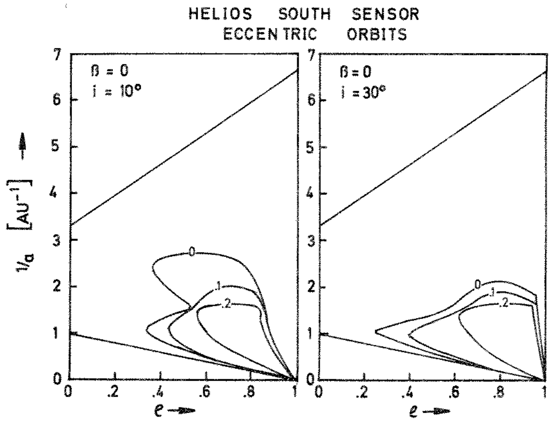

FIG. 12. OBSERVATION PROBABILITY OF "ECCENTRIC" PARTICLES BY THE SOUTH SENSOR.

"eccentric" particles. "Apex" particles can penetrate the film, as has been demonstrated also by the *Pioneer 8* and *9* experiments (Berg and Grün, 1973), while "eccentric" particles did not penetrate the Helios film. In the next chapter it will be discussed what particle property of the "eccentric" particles may cause the observed cut-off.

7. PARTICLE PROPERTIES

The only qualitative difference between the ecliptic and south sensor is the entrance film at the ecliptic sensor. This aluminium coated parylene film has an equivalent thickness of 56 μg/cm^2. The difference in the apertures of both sensors (sensitive area and effective solid angle) can account only for an excess of impacts onto the south sensor of 60%. This cannot explain the difference of observed "eccentric" particles: 3 by the ecliptic sensor and 60 by the south sensor. All the other instrumental characteristics are the same: the electronic charge sensitivities differ by less than 10%, the instrumental dead-times are identical, and the criteria for impact identification are the same for both sensors.

Calibration of the Helios sensors with artificially accelerated iron particles has shown no effect of the entrance film observable in the data, even for dust particles at the sensitivity threshold. First, a thorough investigation of penetration effects by Pailer and Grün (1980) succeeded in identifying the penetration limit of the Helios film.

Simulation experiments with projectiles of various densities ρ like iron ($\rho = 7.9$ g/cm^3), aluminium ($\rho = 2.7$ g/cm^3), glass ($\rho = 2.4$ g/cm^3) and polyphenylene ($\rho = 1.25$ g/cm^3) showed that only polyphenylene particles at an angle of incidence $\alpha = 60°$ ($\alpha = 0°$ is normal to the film) did not penetrate the film. From this result it was concluded that the penetration limit strongly depends on the particle density. A comparison with other penetration and impact crater experiments led to an empirical penetration formula for the Helios film:

$$T = C\rho^{0.33}\, m^{0.40}(v \cos \alpha)^{0.88} \qquad (11)$$

with T the thickness of the film in cm, $T_{Helios} = 3.8 \times 10^{-5}$ cm, $C_{Helios} = 0.93$, ρ is the density of the projectile material in g/cm^3, m is the projectile mass in grams and ($v \cos \alpha$) is the component of the impact speed perpendicular to the film in km/sec. This penetration formula is similar to that which was derived by penetration experiments with mm-sized projectiles by Fish and Summers (1965) and which was applied by Nauman *et al.* (1969) to penetration experiments in the sub-millimetre range. The Fish–Summers penetration formula had to be amended by a correction function in order to describe also experiments with projectiles in the micron and submicron range.

Since the angle of incidence α is not known for individual micrometeoroid impacts better than within the total field of view of the sensor, it can be calculated only on a statistical basis. For an isotropic influx of particles onto the ecliptic sensor, half of the observed particles will have an angle of incidence of $\alpha \leqslant 27°$ and the other half will have $\alpha > 27°$. Taking into account that the trajectory elevations are concentrated towards the ecliptic plane and the sensor axis has an elevation of 25° the average angle of incidence $\bar{\alpha}$ is shifted to $\bar{\alpha} \sim 36°$. With this value set in equation (11), it follows that a dust particle with mass m (g), density ρ (g/cm^3) and impact speed v (km/sec) that satisfies the condition

$$\rho^{0.83} m v^{2.2} > 1.7 \times 10^{-11} \qquad (12)$$

will penetrate the Helios film. On the other hand, dust particles which do not satisfy this condition will not penetrate the film and are not observable by the ecliptic sensor.

This information on the dust particles can be compared with the other information available from the experiment. One direct measurement is the total charge released upon impact. Calibration of the sensors with iron projectiles yielded a dependence of the positive charge Q (C) on the projectile mass m (g) and speed v (km/sec) according to equation (9). Both Dalmann *et al.* (1977) and Pailer and Grün (1980) extended the range of projectile materials which were used for the calibration of the

Helios experiments including low density materials ($\rho \sim 1$ g/cm^3). Their data suggest that at impact speeds of 20–40 km/s (this range includes the most probable impact speed of interplanetary dust particles onto the Helios sensors) the charge yield will not deviate from the charge yield of iron projectiles by more than a factor order of 10. No systematic effect of the charge yield with the projectile density has been observed. Since the mass and speed dependence of the penetration limit and the charge yield are similar, both equations (9) and (12) can be directly compared. If both equations are adjusted at $v = 20$ km/s, which is close to the average impact speed onto Helios, the small difference in the speed dependence can be neglected. It follows from (9) and (12) a relation between the particle density (g/cm^3) and the positive charge yield (C) of particles at the penetration limit:

$$\rho = 4 \times 10^{-18} Q^{-1.2}. \tag{13}$$

A particle population which cannot penetrate the film in front of the ecliptic sensor but which has been observed by the south sensor producing the positive charge Q must have densities below the density calculated from equation (13). Two ways have been shown to identify this population. Firstly, by assuming that the detection probability for both sensors is equal for particles of this population, then the excess of particles observed by the south sensor over the particles observed by the ecliptic sensor constitutes that population. Figure 13 shows that pulse height distrubution which was derived by substracting the number of impacts on the ecliptic sensor from that of the south sensor. Impacts with pulse height numbers $IA = 7$ and 8 were more abundant at the ecliptic sensor, therefore they show negative numbers. The excess of impacts is not only limited to small pulse heights but shows a significant number even at high pulse heights. The total number of the "surplus" particles on the south sensor amounts to 64 impacts.

Secondly, a more direct identification of particles, which did not penetrate the film in front of the ecliptic sensor is for the "eccentric" particles assuming they are equally observable by both sensors. Figure 14 shows the pulse height histogram of the "eccentric" particles observed by the south sensor. Their total number is 60 impacts. Since the total numbers and the pulse height distributions of the "surplus" and the "eccentric" particles are

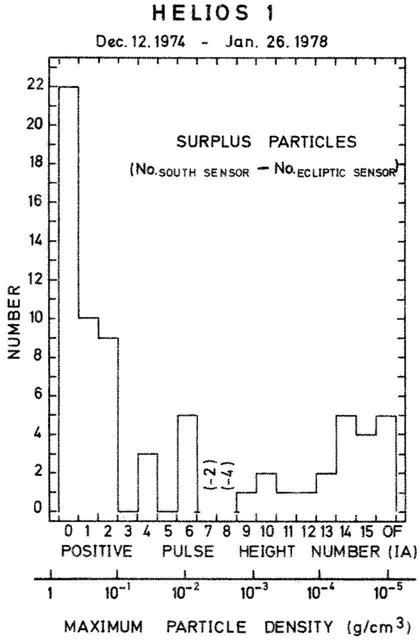

Fig. 13. Pulse height distribution of the excess of impacts onto the south sensor with regard to impacts onto the ecliptic sensor.

The density scale corresponds to projectile densities at the penetration limit of the Helios film ($v = 20$ km/sec). This scale represents an extrapolation of an empirical penetration formula.

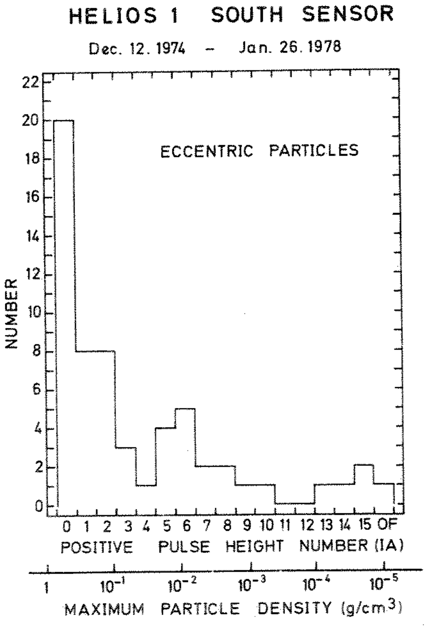

Fig. 14. Pulse height distribution of the "eccentric" particles observed by the south sensor.

For further explanations see Fig. 13.

similar it is concluded that both data represent the same population. For both pulse height distributions density scales according to equation (13) are given which represent the maximum density particles can have. There are about 20 "surplus" and "eccentric" particles with pulse height numbers $IA \geq 4$ which correspond to density $\rho < 0.1$ g/cm^3. Twenty excess particles of both types can be considered as a significant number with respect to the total number of impacts observed by Helios. They amount to approximately 30% of all "eccentric" particles. Taking into account the uncertainty of the density determination by the above method of approximately a factor of 10 it is concluded that a significant number of interplanetary dust particles with densities $\rho < 1$ g/cm^3 have been found by the Helios experiment. The very low densities indicated for large pulse height numbers are considered to be spurious because they represent huge extrapolations from the experimental data.

8. CONCLUSIONS

Two different types of interplanetary dust particles have been identified by the Helios experiment. They differ in their orbital characteristics and in their material properties with respect to the penetration of a thin film. Only directly measured parameters, like sensor azimuth and spacecraft true anomaly at the time of impact and total charge released upon impact, have been used for the identification of the two particle populations. Therefore this identification is free of any uncertainty of the type which is introduced when an empirical calibration is applied in order to derive a physical parameter (e.g. particle mass or impact speed) from a measured quantity. Only the derivation of the particle densities involved the calibration of the total charge and the penetration limit with respect to particle mass, speed and density. The results from this analysis contain some uncertainties therefore only upper/lower limits of densities are given.

"Apes" particles are recognized by the direction from which they impacted onto the sensors. The ecliptic sensor observed just this population. This signature alone limits the range of orbital elements to eccentricities $e < 0.4$ or semi-major axes $a \leq 0.5$ *AU*. Large impacts (pulse height $IA > 2$) show a concentration towards the ecliptic plane with an average inclination $\bar{i} < 30°$. Since these "apex" particles did penetrate the Helios film the density given by equation (13) is a lower limit of their densities. This lower limit ($\rho > 1$ g/cm^3) is no severe restriction as normal meteoritic materials ($\rho > 2$ g/cm^3) meet this requirement. This density limit for the particles which penetrated the film may be even further lowered by the fact that these dust particles produce less charge after the penetration than they would have produced without the penetration (Pailer and Grün, 1980). Therefore only very fluffy structures ($\rho < 0.1$ g/cm^3) may be excluded for the smallest impacts. "Apex" particles have also been identified by other space experiments like *Pioneer 8/9* (Berg and Gerloff, 1971 and Berg and Grün, 1973) and HEOS-2 (Hoffmann *et al.* 1975b). Therefore it is concluded that they constitute a common class of micrometeoroids which can be found throughout the inner solar system from at least 0.3 to 1 *AU*. An explanation for their orbital characteristics has been given by Grün and Zook (1980).

The second population of micrometeoroids is identified by the fact that they did not penetrate the film in front of one of the Helios sensors (ecliptic sensor) and hence were only observed by the south sensor. The excess of impacts on the south sensor showed an azimuthal distribution which depart from that of the "apex" particles. These particles were called "eccentric" particles because their orbits must have eccentricities $e > 0$. A more detailed analysis showed that they have even eccentricities of $e > 0.4$ and semimajor axes $a > 0.5$ *AU*. The portion of this particle population on those impacts detected by the south sensor from the apex direction is unknown. Part of the particles from the apex direction, at least, must belong to the "eccentric" particle population, because some fraction of the possible impact configurations (both Helios and particle inbound and vice versa) lead to small azimuth angles and hence these impacts would be observed from the apex direction.

Hyperbolic orbits are directly recognized from the statistically significant imbalance of outgoing and ingoing particles. This surplus of outgoing particles has been known also from the *Pioneer 8* and *9* experiments (Berg and Grün, 1973) and was identified by Zook and Berg (1975) as particles (β-meteoroids) which are produced by collisions of bigger meteoroids in the inner solar system. By the action of radiation pressure they are expelled from the solar system on hyperbolic orbits. These β-meteoroids were much more prominently seen by the *Pioneer 8* and *9* experiments than by the Helios south sensor. This might be the effect of their inclination distribution or the effect of their interaction with the interplanetary magnetic field (Morfill and Grün, 1979a, b).

An analysis of the Helios data, taking into account the measured impact speeds by Schmidt and Grün (1979), showed that part of the particles detected are on hyperbolic orbits, apart from the β-meteoroids. Even from the data presented here it is suggested that part of the "eccentric" particles are on hyperbolic orbits, both outbound and inbound. Inbound particles on hyperbolic orbits do not necessarily imply their interstellar origin but also collisions of larger meteoroids or evaporation of comets may have produced these particles outside the orbit of Helios. Also dust particles released from ancient solar comets on their repeated appearance in the inner solar system may contribute to this population, although they will not be distinguishable from interstellar dust. The "eccentric" particle population-besides the β-meteoroids-are not so prominently observed in the data from the *Pioneer 8* and *9* and HEOS-2 experiments. Both experiments observed from the antapex direction only half the impact rate than from the apex direction (Fechtig, 1976, Berg and Grün, 1973). This may be due to the different observation geometries and to the long-term change in the interplanetary magnetic field configuration as proposed by Morfill and Grün (1979a, b).

Collection experiments of extraterrestrial dust in the upper atmosphere (e.g. Brownlee *et al.* 1977 and Brownlee, 1978) showed that a considerable fraction of the particles-even of the small particles with 1–10 μm in diameter-are of fluffy structure, aggregated of many very small particles, sometimes as small as 0.2 μm in diameter. This suggests low bulk density of the whole particles although to our knowledge it has never been determined directly. Crater investigations on lunar samples (Nagel *et al.* 1975) showed that there exists a population of micrometeoroids with densities of the order of $\rho \sim 1\,\mathrm{g/cm^3}$. This was derived from the existence of very shallow craters which could not be generated by stony or iron micrometeoroids. In order to explain the observed polarization of the zodiacal light Giese *et al.* (1978) require the contribution of fluffy interplanetary particles. For particles in the larger size regime meteor observations confirmed that there are especially comet related meteors with densities down to $0.2\,\mathrm{g/cm^3}$ (Ceplecha, 1976 and 1977).

The combination of a penetration experiment and an impact plasma detector in the Helios experiment for the first time allowed the determination of the bulk density together with other physical and dynamical characteristics of micrometeoroids. For approx. 30% of the "eccentric" particles a bulk density of $\rho < 1\,\mathrm{g/cm^3}$ was derived. This number includes a margin of a factor of 10 for the uncertainty of the chemical composition. This low density of "eccentric" particles supports their relationship to comets. High eccentricities and low bulk densities are known for meteor stream particles (Ceplecha, 1977) and sporadic meteors (Sekanina and Southworth, 1975) which are directly related to comets. Future considerations of other data obtained by the Helios experiment like mass, impact speed and information on chemical composition of the detected particles will further narrow down the range of orbital characteristics and material properties of the different interplanetary dust populations.

Acknowledgements—The cooperation with G. Braun, B. -K. Dalmann, P. Gammelin, O. Kress, D. Linkert and W. Schneider during the successful development, implementation, calibration and operations of the Helios experiments is gratefully acknowledged. Important suggestions were made by G. Morfill and H. Zook. The computations were supported by G. Dräger and M. Leistner.

This work was supported by the Bundesminister für Forschung und Technologie.

REFERENCES

Berg, O. E. and Gerloff, U. (1971). More than two years of micrometeorite data from two Pioneer Satellites. *Space Res.* **XI,** 225

Berg, O. E. and Grün, E. (1973). Evidence of hyperbolic cosmic dust particles. *Space Res.* **XIII,** 1046.

Briggs, R. E. (1962). Steady-state space distribution of meteoritic particles under the operation of the Poynting–Robertson effect. *Astron. J.* **67,** 710.

Brownlee, D. E. (1978). Microparticle studies by sampling techniques. *Cosmic Dust* (Ed. J. A. M. McDonnell), Wiley, Chichester, p. 275.

Brownlee, D. E., Rajan R. S. and Tomandl D. A. (1977). Chemical and textural comparison between carbonaceous chondrites and interplanetary dust. *Comets Asteroids Meteorites. Interrelations, Evolution and Origins* (Ed. A. H. Delsemme), p. 137. Univ of Toldeo.

Ceplecha, Z. (1976). Fireballs as an atmospheric source of meteoritic dust. *Lecture Notes Phys.* **48,** 385.

Ceplecha, Z. (1977). Meteoroid populations and orbits. *Comets Asteroids Meteorites. Interrelations, Evolution and Origins* (Ed. A. H. Delsemme), p. 143. Univ of Toledo.

Dalmann, B. -K., Grün E. and Kissel J. (1977). The ion composition of the plasma produced by impact of fast particles. *Planet. Space Sci.* **25,** 135.

Dietzel, H., Eichhorn G., Fechtig H., Grün E., Hoffmann H. J. and Kissel J. (1973). The HEOS-2 and Helios micrometeoroid experiments. *J. phys. E. Sci. Instrum.* **6,** 209.

Dohnanyi, J. S. (1976). Flux of hyperbolic micrometeoroids. *Lecture Notes Phys.* **48,** 170.

Fechtig, H. (1976). In-situ records of interplanetary dust particles—methods and results. *Lecture Notes Phys.* **48,** 143.

Fechtig, H., Grün, E. and Kissel, J. (1978). Laboratory simulation. *Cosmic dust* (Ed. J. A. M. McDonnel), p. 607. Wiley, Chichester.

Fish, R. H. and Summers, J. L. (1965). The effects of material properties on threshold penetration. *Proc. 7th Hypervelocity Impact Symp.* **3,** 2.

Giese, R. H., Weiss, K., Zerull R. H. and Ono T. (1978). Large fluffy particles: a possible explanation of the optical properties of interplanetary dust. *Astr. Astrophys.* **65,** 265.

Grün, E., Fechtig, H., Gammelin, P., Kissel, J., Auer, S., Braun, G., Dalmann, B.-K., Dietzel, H. and Hoffmann, H. J. (1979). Das Helios-Micrometeoritenexperiment. *BMFT-FB* W79-09.

Grün, E., Fechtig, H., Kissel, J. and Gammelin, P. (1977). Micrometeoroid data from the first two orbits of Helios 1. *J. Geophys.* **42,** 717.

Grün, E. and Zook, H. A. (1980). Dynamics of micrometeoroids in the inner solar system. Solid Particles in the Solar System in *Proc. IAU Symp.* 90 (Ed. I. Halliday and B. A. McIntosh).

Hoffmann, H. J., Fechtig, H., Grün, E. and Kissel, J. (1975a). First results of the micrometeoroid experiment S215 on the HEOS-2 satellite. *Planet. Space Sci.* **23,**215.

Hoffmann, H. J., Fechtig, H., Grün, E. and Kissel, J. (1975b). Temporal fluctuations and anisotropy of the micrometeoroid flux in the Earth–Moon–system. *Planet. Space Sci.* **23,** 985.

Leinert, C., Hanner, M., Richter, I. and Pitz, E. (1979). The plane of symmetry of interplanetary dust in the inner solar system. *Astr. Astrophys.* In press.

Leinert, C., Pitz, E., Hanner, M. and Link, H. (1977). Observations of zodiacal light from Helios 1 and 2. *J. Geophys.* **42,** 699.

Link, H., Leinert, C., Pitz, E. and Salm, N. (1976). Preliminary results of the Helios A zodiacal light experiment. *Lecture Notes Phys.* **48,** 24.

McDonnell, J. A. M. (1978). Microparticle studies by space instrumentation. *Cosmic Dust* (Ed. J. A. M. McDonnell), p. 337. Wiley, Chichester.

McDonnell, J. A. M., Berg, O. E. and Richardson, F. F. (1975). Spatial and time variations of the interplanetary microparticle flux analysed from deep space probes Pioneers 8 and 9. *Planet. Space Sci.* **23,** 205.

Morfill, G. E. and Grün, E. (1979a). The motion of charged dust particles in interplanetary space. I. The zodiacal dust cloud. *Planet. Space Sci.* **27** 1269.

Morfill, G. E. and Grün, E. (1979b). The motion of charged dust particles in interplanetary space. II. Interstellar grains. *Planet. Space Sci.* **27,**1283.

Nagel, K., Neukum, G., Eichhorn, G., Fechtig, H., Müller, O. and Schneider, E. (1975). Dependencies of microcrater formation on impact parameters. *Proc. 6th Lunar Sci. Conf.* 3417.

Naumann, R. J., Jex, D. W. and Johnson, C. L. (1969). *Calibration of Pegasus and Explorer XXIII detector panels.* NASA Technical Report R-321.

Öpik, E. (1951). Collision probabilities with the planets and the distribution of interplanetary matter. *Proc. R. Irish Acad.* A **54,** 165.

Pailer, N. and Grün, E. (1980). The penetration limit of thin films. *Planet. Space Sci.* **28,** 321–331.

Rhee, J. W., Berg, O. E. and Richardson, F. F. (1974). Heliocentric distribution of cosmic dust intercepted by Pioneer 8 and 9. *Geophys. Res. Lett.* **1,** 345.

Röser, S. (1976). Can short period comets maintain the zodiacal cloud?. *Lecture Notes Phys.* **48,** 319.

Schmidt, K. D. (1977). Micrometeoroid orbits observable by the Helios micrometeoroid detector (E10). *J. Geophys.* **42,** 737.

Schmidt, K.D. and Grün, E. (1979). The distribution of orbital elements of interplanetary dust in the inner solar system as detected by the Helios space probe. *Space Res.* **XIX,** 439.

Schwehm, G. and Rhode, M. (1977). Dynamical effects on circumsolar dust grains. *J. Geophys.* **42,** 727.

Sekanina, Z. and Southworth, R. B. (1975). Physical and dynamical studies of meteors. Meteor-fragmentation and stream-distribution studies. NASA Contractor Report CR-2615.

Singer, S. F. and Bandermann, L. W. (1967). Nature and origin of zodiacal dust. NASA SP-150, 379.

Southworth, R. B. and Sekanina, Z. (1973). Physical and dynamical studies of meteors. NASA Contractor Report CR-2316.

Whipple, F. L. (1955). A comet model, III. The zodiacal light. *Astrophys. J.* **121,** 750.

Zook, H. A. (1975). Hyperbolic cosmic dust: its origin and its astrophysical significance. *Planet. Space Sci.* **23,** 1391.

Zook, H. A. and Berg, O. E. (1975). A source for hyperbolic cosmic dust particles. *Planet. Space Sci.* **23,** 183

```
(  200)  4051AABB  0D404647  2D074069  E8380740  5DF8360F  01800000  06008000  00054053  74BA054C  44ECFD03
(  240)  406C2C55  05406124  49070180  00000600  80000005  404C1480  0B40440A  150F4070  E6540D40  6CF7C962
(  280)  01800000  06008000  00054048  7720073F  EECECC04  4075D7D6  0F4063AD  F4050180  00000600  80000005
(  320)  404BFEAA  0E3FF420  F106406D  16F58D40  5DE0460F  01800000  06008000  00053FF2  C5E2003F  7E135F0C
(  360)  40504CE0  0B40485F  5C000180  00000600  80000005  3FEA7645  0B3F6D15  A103405C  10240740  54711404
(  400)  01800000  06008000  00054042  2061093F  C3FE890E  405CE176  0F405069  5C060180  00000600  80000005
(  440)  3FE489CB  003F66A3  690C4058  BA060140  4B78C608  01800000  06008000  00053FE9  E6CC0D3F  6A163D05
(  480)  40486BBD  09404326  F0010180  00000600  80000005  3FFE4720  0F3FC045  7A074059  31700440  52E7E20F
(  520)  01800000  06008000  00054053  02810D3F  D4DEEA05  406CB030  0E406194  12040180  00000600  80000005
(  560)  405A0621  043FDBD9  61084068  F2460440  5BA77F04  01800000  06008000  00054052  7D46003F  6206ED09
(  600)  406C5F14  0E4058AE  770C0180  00000600  80000005  3FD90E92  0C30DEF7  A5014066  17990B40  43E7400B

FILE     1  RECORD        5  LENGTH      640BYTES
(    0)  01000000  01018000  00070080  0000053F  CF8CF607  3DCA730E  0140684D  0F023FF7  23510E01  80000006
(   40)  00800000  053FF23A  40063DDB  27D20840  6FA39A02  40550083  0F018000  00060080  00000540  5354250B
(   80)  3FCEDD69  0D406D1E  F7004064  071C0C01  80000006  00800000  05405055  89003FD2  E4E00E40  7585E30B
(  120)  406DCDB8  05018000  00060080  00000540  5BB13E0A  3FDFAC05  044072C4  1000406E  16FE0901  80000006
(  160)  00800000  0540645E  C5023FEA  16F20340  791EBD0E  406E54E7  0C018000  00060080  00000540  5C0B2704
(  200)  3FE08C12  08407625  1A0A4067  DA980001  80000006  00800000  053FFB25  550E3F7D  9ED70A40  77439C02
(  240)  4068F409  04018000  00060080  00000540  464E7602  3FC7B66E  054079D1  3A0B4069  0EA00501  80000006
(  280)  00800000  053E6CB4  85023DEE  E117023E  F437CA01  3EE0D8C9  04018000  00060080  00000540  40DF1B09
(  320)  3FC22B3F  0F40768B  0307406A  EA130A01  80000006  00800000  05404093  FF083FC1  DEA39D40  72EA0900
(  360)  40679D70  0A018000  00060080  0000053F  EDAEBA02  3F6FE04D  03407483  44024065  62840F01  80000006
(  400)  00800000  0540490C  030C3FCA  82030D40  7C248D09  4070A949  07018000  00060080  0000053F  EAC9950E
(  440)  3F6CE328  04406EAB  89084060  F35D0C01  80000006  00800000  053F4753  4E093EC9  C07E033F  CD79C800
(  480)  3FC29277  0C018000  00060080  0000053F  654D940B  3EE75440  0A4054FF  FC0F404A  05340F01  80000006
(  520)  00800000  053FD224  1B093ED2  634D0E40  727BEE00  405C9EC4  0F018000  00060080  0000053F  53604402
(  560)  3D7FB211  0E405963  DE083FDB  AA4D0601  80000006  00800000  053F69FF  87043D77  E5020D40  6A05E70A
(  600)  3FFDCEE5  02018000  00060080  0000053E  FB6A3E0D  3CFB26CB  00406D84  3805404A  D4310401  80000006

FILE     1  RECORD        6  LENGTH      640BYTES
(    0)  00800000  053FF5AC  90063F76  756A0A40  692B340B  405096D4  03018000  00060080  0000053F  FFC0E007
(   40)  3FC1F9F4  0A405B75  95074051  9E3C0201  80000006  00800000  05404AB9  F5003FCC  661F0040  6B8F9304
(   80)  405FE7F6  0D018000  00060080  00000540  44757C00  3FC612BB  06406DE8  5E02405E  916A0301  80000006
(  120)  00800000  05404F86  D80D3FD1  76920E40  6D387109  40601E55  0E018000  00060080  00000540  51249104
(  160)  3FD46ADF  05407857  520A4067  E8C10601  80000006  00800000  053EE7EB  E4063E6A  4A2D053F  511F6C09
(  200)  3EFC45B1  09018000  00060080  00000500  00000000  00000000  00000000  00000000  00000001  80000006
(  240)  00800000  05000000  00000000  00000000  00000000  00000000  00018000  00060080  00000500  00000000
(  280)  00000000  00000000  00000000  00000001  80000006  00800000  053FE3AC  850F3F65  9E3C0940  45EF3609
(  320)  3FFBAC6F  06018000  00060080  00000540  4B399F06  3FCCB7A7  0640700F  9E0C4063  44F20801  80000006
(  360)  00800000  05404E44  29023FCF  C8850940  6FDC970B  406519DB  05018000  00060080  0000053F  DC3FAE07
(  400)  3F5E1211  0240407D  8F0F3FED  FF6C0901  80000006  00800000  053FE1C9  000D3F63  D5E6963F  F3EFC207
(  440)  3FE39790  0E018000  00060080  0000053F  71BBFB06  3EC49E88  0A405AF8  D70A4047  08FF0E01  80000006
(  480)  00800000  053F58B0  0A0C3DC0  717C0540  6D4EB104  3FF7FFED  08018000  00060080  0000053E  CA735907
(  520)  3CECFE45  0D4072F0  D6013FE0  0D050001  80000006  00900000  053F4743  56053D52  2FD50D40  6CFEA73E
(  560)  405023EA  0D018000  00060080  0000053F  C6255400  3F45165E  054074E1  9E064066  FCA3C301  80000006
(  600)  00800000  053FC106  14023F42  53000140  75A6C90F  40652021  05018000  00060080  0000023E  E7459501

FILE     1  RECORD        7  LENGTH      640BYTES
(    0)  01000000  043F6956  5509405C  C3CB0540  555CA70A  01800000  07008000  00053FF3  17F4003F  75653B07
(   40)  406DEB2C  00406272  6C050180  00000600  80000005  3FE28F97  003F6488  38004055  F7F20440  4C0C870A
(   80)  01800000  06008000  00050000  00000000  00000000  00000000  00000000  00000180  00000600  80000005
(  120)  00000000  00000000  00000000  00000000  00000000  01800000  06008000  00050000  00000000  00000000
(  160)  00000000  00000000  00000180  00000600  80000005  00000000  00000000  00000000  00000000  00000000
(  200)  01800000  06008000  00050000  00000000  00000000  00000000  00000000  00000180  00000600  80000005
(  240)  00000000  00000000  00000000  00000000  00000000  01800000  06008000  00053FCA  5EB1013F  4C19AF08
(  280)  40477053  0040415C  A2090180  00000600  80000005  3FEA0663  0C3F6A18  04014056  A0650340  57E34E00
(  320)  01800000  06008000  00053F68  F8DC063E  EE125106  406F0CB8  0A4063F2  3A0A0180  00000600  80000005
(  360)  3FC5A3E8  0D3F4708  770B406D  81130940  61D2130C  01800000  06008000  00053F5A  0551013E  C44EA20C
(  400)  4078EF91  0440580B  7C0F0180  00000600  80000005  3F43D6AE  043CF090  F0013F66  5B08003F  4E042108
(  440)  01800000  06008000  00053E46  9141013D  4FA16007  40425914  013FC8FC  06060180  00000600  80000005
(  480)  3F4B70F3  043DC5B6  93014061  60C10340  50707108  01800000  06008000  00053FCA  4EA9C43F  4A20CA02
(  520)  407C0D87  0A406FF3  100F0180  00000600  80000005  3FF555A8  0F3F77AE  6C0E4070  E1340740  6A91CF0F
(  560)  01800000  06008000  00054043  A8F20F3F  C4F16A0C  407CA9D4  0F407540  11C70180  00000600  80000005
```

Helios-A
12/19/74 - 1/02/80

```
                         DUMP OF TAPE HELIOS

  INPUT TAPE  HELIOS  ON  MT4
  DATA INPUT     H9 FL 1 15 STOP

  FILE       1  RECORD        1  LENGTH     640BYTES
   (      0)  00800000  05406418  73083F64  9F5E0C40  7B16C30C  405F6F5C  06018000  00060080  00000540  6F26170D
   (     40)  3FC77CCC  06407C8C  2A0C4062  A2D00D01  80000006  00800000  05406030  090F3F7C  2520C040  70601D04
   (     80)  4068E69C  08018000  00060080  00000540  5FB8510B  3F65F1E4  07407566  0E014058  E6950701  80000006
   (    120)  00800000  05000000  00000000  00000000  00000000  00000000  00018000  00060080  00000540  48C10F0C
   (    160)  3EEEEFEC  03404F43  1D013FF7  68C50101  80000006  00800000  05404A29  140E3EDE  0FF30A40  50C5EF0D
   (    200)  40518013  07018000  00060080  00000540  461D7603  3DFE5ACF  06405A58  9C0D404A  E2030B01  80000006
   (    240)  00800000  053FF5AA  050D3E6D  6E640140  656A4603  40515137  08018000  00060080  0000053F  0565E000
   (    280)  3ED6AFEC  094071D3  CA0C405A  A17C0301  80000006  00800000  0540610A  E001405A  CCC70340  6A5E6404
   (    320)  405F3220  01018000  00060080  00000540  5986970F  4051C8CF  08407025  260C4063  E3C10701  80000006
   (    360)  00800000  05404603  23003FDC  E5140440  6A17B804  4062387E  01018000  00060080  0000053E  [illegible]
   (    400)  3D45203C  083DE61D  280E3DCA  932F0301  80000006  00800000  053D6869  E5023CEA  E07E033D  [illegible]
   (    440)  3D5C5B55  08018000  00060080  0000053E  541F7305  3D0A6696  0F3E5CDC  E80C3E4C  C8E0CA01  80000006
   (    480)  00800000  053F7DB4  70033F41  F38D063F  D386F901  3FCA8C6F  0F018000  00060080  0000053F  45716F01
   (    520)  3F786AE1  0E4059E4  45044053  65A40601  80000006  00800000  053FED4A  630C3FCE  21BCCC40  70DAE502
   (    560)  40648EF9  02018000  00060080  0000053F  01683405  3FC61F22  00405284  FB004042  6D3C0501  80000006
   (    600)  00800000  053FF2B6  8D0A3FE8  C57C0640  4FB4E500  4041DF07  08018000  00060080  000C0240  [illegible]

  FILE       1  RECORD        2  LENGTH     640BYTES
   (      0)  01000000  0440461F  E70E406A  FA820740  5E41B508  01800000  07008000  0005404F  FDC90640  41EEC301
   (     40)  406460A2  0A405DC2  10050180  00000600  80000005  405C6043  0D40401B  C1CC406A  6B5E0640  6314110F
   (     80)  01800000  06008000  00054058  4B500D40  51683A05  40643D28  02405900  1C060180  00000600  80000005
   (    120)  3EC5CA4A  0A3E6EAA  910D3ED4  9D94063E  CDD1E70F  01800000  06008000  00053F5C  E2240A3E  E4251A09
   (    160)  3FE3BA24  073FD19A  12030180  00000600  80000005  3FF5D203  083E660E  D90B4071  6EE80340  5520C304
   (    200)  01800000  06008000  00053FED  90F4053E  C0EBA109  40798B60  04405ED8  3ECE01A0  00000600  80000005
   (    240)  404046FF  043FCE9C  06024068  F2950340  5EC8C406  01800000  06008000  00053FFE  3960043F  E11F4107
   (    280)  4058D771  09405025  CB000180  00000600  80000005  4948A037  003FE941  85064060  22960F40  5F33BD13
   (    320)  01800000  06008000  00054048  2C62053F  ED821F00  40654D0B  0740579E  7A0DC180  00000600  80000005
   (    360)  404EE38F  033FF20A  33004079  E22E0440  69D03A08  01800000  06008000  00054041  150A023F  D9C7119E
   (    400)  407663CA  0240683B  D7020180  00000600  80000005  3FF06644  073FC9E2  B197406F  875E0C40  61AA7F04
   (    440)  01800000  06008000  00053FF2  A9CD033F  D5E15109  406EE004  0F40626A  220F0180  00000600  80000005
   (    480)  3FFCFE5D  013FE2A5  AB044076  FE910A40  65090290  01800000  06008000  00053FFF  D3C10A3F  D3A3D605
   (    520)  406BAC16  0C405873  B7020180  00000600  80000005  3FC7F270  0E3F5210  66023FFC  A673043F  EC8492DF
   (    560)  01800000  06008000  00053FC8  2FC20D3F  56FE2E03  40497567  0F4040DA  65610180  00000600  80000005
   (    600)  40418F68  003FD3F3  08034076  72760E40  67652006  01800000  06008000  00033FDF  4D63303F  7A55CE05

  FILE       1  RECORD        3  LENGTH     640BYTES
   (      0)  01000000  034061EC  E807405A  6C850A01  80000007  00800000  053FD6D3  E6033FC1  C6DC033F  E4654105
   (     40)  3FDC7AAB  09018000  00060080  0000053F  CEDE0006  3FC85FCE  063FEE3A  B1023FDD  B7970001  80000006
   (     80)  00800000  053FE972  96053FD3  16850F40  5A5F0605  4048944C  02018000  00060080  0000053F  C4F05605
   (    120)  3E5996FA  0A4055EB  05033FF9  A6D30201  80000006  00800000  053FD206  E6023DE0  4008C940  6FF81D0C
   (    160)  404FF7AD  08018000  00060080  00000540  43496F06  3FD320F1  03407853  B8054065  0CEF0501  80000006
   (    200)  00800000  054049AB  40003FF4  26C60A40  7E072D03  40730393  09018000  00060080  0000053F  FFFD6301
   (    240)  3FD8130A  0E407471  D7014066  57F10601  80000006  00800000  054048E5  640A3FE0  FEEC0E40  6C05710F
   (    280)  40615D74  02018000  00060080  0000053F  FAA76009  3FD234AD  03405F0D  4B0D4057  5DA60301  80000006
   (    320)  00800000  053FF903  FE053FD0  06830240  6A962E0A  40645B7C  04018000  00060080  0000053F  0C012700
   (    360)  3F73454E  07406A93  B0014061  A5FB0801  80000006  00800000  053FD95A  C70D3F68  39850740  4E4C4009
   (    400)  404649F8  0D018000  00060080  0000053F  FC13C700  3FDD9A6B  0E406700  6C09405F  752D0301  80000006
   (    440)  00800000  053FED56  04043FC9  59D60F40  6882460A  4061C124  03018000  00060080  00000540  4623E304
   (    480)  3FD14A1B  0B4065D7  64004060  06E10401  80000006  00800000  053FC58A  FF003F65  58960740  40C2EC0F
   (    520)  3FF8B2E2  01018000  00060080  0000053E  EFD2EC0E  3EE7475A  053EF911  97093EE1  2D6A0C01  80000006
   (    560)  00800000  053ED5A8  FF033ECF  F5CF023E  D8CC850E  3ED81070  08018000  00060080  0000053F  E5856804
   (    600)  3FC48EA7  0E4040AC  7D003FFA  45130201  80000006  00800000  04404080  DC0B3EC4  80400840  56E8F80A

  FILE       1  RECORD        4  LENGTH     640BYTES
   (      0)  01000000  02404FE2  24070180  00000700  80000005  3FC13488  063F4E26  FF053FD0  85740F3F  CF10D506
   (     40)  01800000  06008000  00053FCD  7148033E  D356F307  4076A6E9  03405786  DA0D0180  00000600  80000005
   (     80)  3FDCF29F  083DEC8A  9C0C4064  B13C0C40  484A710F  01800000  06008000  00053FD0  C9CF013F  4141E604
```

```
FILE       1  RECORD       8  LENGTH     640BYTES
(      0)   01000000  03406E4D  A9004067  DD060001  80000007  00800000  05000000  00000000  00000000  00000000
(     40)   00000000  00018000  00060080  00000500  00000000  00000000  00000000  00000000  00000001  80000006
(     80)   00800000  05000000  00000000  00000000  00000000  00000000  00018000  00060080  00000500  00000000
(    120)   00000000  00000000  00000000  00000001  80000006  00800000  05000000  00000000  00000000  00000000
(    160)   00000000  00018000  00060080  00000500  00000000  00000000  00000000  00000000  00000001  80000006
(    200)   00800000  05000000  00000000  00000000  00000000  00000000  00018000  00060080  00000500  00000000
(    240)   00000000  00000000  00000000  00000001  80000006  00800000  05000000  00000000  00000000  00000000
(    280)   00000000  00018000  00060080  0000053F  7733C608  3EF99617  03404127  94023EF8  C7C40101  80000006
(    320)   00800000  053F51AD  C5013E54  ADC60040  7944200E  4050B1D9  06018000  00060080  0000053F  44EE3D06
(    360)   3D76B550  0E40617A  E30F3FF9  4D460701  80000006  00800000  053E5E63  130F3CD8  BCBE0340  42AEE906
(    400)   3F7C2669  09018000  00060080  0000053D  EFE22D03  3C762288  0340421B  4F093FE7  68660301  80000006
(    440)   00800000  053FCC25  BB0E3F4D  95460E40  6A08860B  4062B436  06018000  00060080  00000540  4254AF01
(    480)   3FC3E993  0D40738B  A608406B  A2410901  80000006  00800000  053FFE72  38063FC0  7C0CC040  72374003
(    520)   406BC90A  06018000  00060080  0000053F  6B161F0F  3EED3A68  043FDE37  EA043FD3  94F40B01  80000006
(    560)   00800000  05000000  00000000  00000000  00000000  00000000  00018000  00060080  00000500  00000000
(    600)   00000000  00000000  00000000  00000001  80000006  00800000  04000000  00000000  00000000  00000000

FILE       1  RECORD       9  LENGTH     640BYTES
(      0)   01000000  02000000  00000180  00000700  80000005  00000000  00000000  00000000  00000000  00000000
(     40)   01800000  06008000  00050000  00000000  00000000  00000000  00000000  00000180  00000600  80000005
(     80)   00000000  00000000  00000000  00000000  00000000  01800000  06008000  00050000  00000000  00000000
(    120)   00000000  00000000  00000180  00000600  80000005  00000000  00000000  00000000  00000000  00000000
(    160)   01800000  06008000  00050000  00000000  00000000  00000000  00000000  00000180  00000600  80000005
(    200)   3ED9A332  063E5B6E  230F3F6D  164B003F  6776BF01  01800000  06008000  00053FDF  21C8003F  613EDB06
(    240)   40701FF3  004068E4  B10C0180  00000600  80000005  3FD12927  0E3ED2F3  620D4073  E7040840  5440FA06
(    280)   01800000  06008000  00053EED  6905093D  64643307  3FE9B6CA  053FCF73  E30F0180  00000600  80000005
(    320)   3F40EB15  0A3D6360  4A0B4065  3E7F043F  F7595608  01800000  06008000  00053FD0  3CAE0730  0259E401
(    360)   4071AA4A  0E40523C  F2030180  00000600  80000005  3FEE3E13  0E3F6AA0  210D4077  E720DF40  6CAC669E
(    400)   01800000  06008000  00053FFC  B410093F  7F34DD05  4072063C  00406A77  C0050180  00000600  80000005
(    440)   40505671  0B3FD1F1  C50E406D  CF3C0C40  677B860D  01800000  06008000  00054040  870E0A3F  C14EE0D0
(    480)   4067922D  05406107  5B050180  00000600  80000005  00000000  00000000  00000000  00000000  00000000
(    520)   01800000  06008000  00050000  00000000  00000000  00000000  00000000  00000180  00000600  80000005
(    560)   00000000  00000000  00000000  00000000  00000000  01800000  06008000  00050000  00000000  00000000
(    600)   00000000  00000000  00000180  00000600  80000005  00000000  00000000  00000000  00000000  00000000

FILE       1  RECORD      10  LENGTH     640BYTES
(      0)   01000000  01018000  00070080  00000500  00000000  00000000  00000000  00000000  00000001  80000006
(     40)   00800000  05000000  00000000  00000000  00000000  00000000  00018000  00060080  00000500  00000000
(     80)   00000000  00000000  00000000  00000001  80000006  00800000  05000000  00000000  00000000  00000000
(    120)   00000000  00018000  00060080  00000500  00000000  00000000  00000000  00000000  00000001  80000006
(    160)   00800000  053EC5EB  CD033E47  51CC023F  D3135604  3FC92D43  06018000  00060080  0000053F  616EC00D
(    200)   3ED9045A  02407DB7  C4054060  1CCC0601  80000006  00800000  053F62EC  B8083EEF  7BE40B40  67EE0B04
(    240)   3FF6AEAB  07018000  00060080  0000053F  63ABF103  3EF68C55  0A405AA6  720B3FD6  E5C00601  80000006
(    280)   00800000  053F42BE  47023E5E  EE300B40  62764B04  40435F53  00018000  00060080  0000053F  CF833400
(    320)   3F514B4A  09407C88  9D0B406C  53E90601  80000006  00800000  053FFEF0  D3023F75  5C0A0A40  5E746A06
(    360)   4056BDD8  0D018000  00060080  00030040  C0000000  43CA0000  0044D840  0000427C  00000043  42C00000
(    400)   43680000  00000000  000041C0  00000042  00000000  43E40000  0026D3AE  6A002945  73E40100  00000000
(    440)   2BC98C4B  0D407D4F  DF0443D3  947A0E44  66A80000  00000000  00437EBA  A70140C0  00000040  C0000000
(    480)   406519A5  023FCF6A  560D3FDB  3DF6013F  C2224D0F  42C6783D  0C427F35  EA0E4071  2912093E  F0E23903
(    520)   405F1315  03404B1D  63084140  00000000  00000000  00000000  0040C000  00004047  8EBA0B3F  5E25ED0A
(    560)   3E4A1FFA  043E4156  26013EE6  3200023E  49850602  3D5D46F5  0930546D  5E0E3D4F  C2290D3D  4930F001
(    600)   3D41121C  073CD078  9A060180  00030100  80000005  41400000  0043CA00  000044D8  00000042  C0000000

FILE       1  RECORD      11  LENGTH     640BYTES
(      0)   01000002  0C42F000  000041C0  00000040  C0000000  42C69FEF  0C42F7D4  13094362  D3C3652E  C4357A0E
(     40)   2CF75DCF  01000000  00002E68  72150340  75F07609  43D7A33E  0644CF74  00000000  00000044  436F5507
(     80)   41600000  0040C000  000040D9  A8230F40  424A960F  40594ED1  0F3F78C4  870B43D4  02070443  5734E507
(    120)   3FE3B835  0A3FD41A  3B0B405A  93AE093F  5EC59C0B  41600000  00000000  00000000  00000041  40000000
(    160)   3EFA0E58  0C3FE417  F6063E64  733D0A3D  63801E06  3DFB0BE1  0C3E6273  F4023DD1  6E5E073E  62C62102
(    200)   3EDEEF79  0F3E6CE9  460E3ECD  ED9A013E  7C4F870F  01800003  02008000  03004160  00000043  C4000000
(    240)   44DB4000  0042CC00  00004268  00000042  C0000000  40C00000  00437249  240943E4  000F0044  57E00000
(    280)   27482A05  02287E49  880F0000  00000029  EE805700  4079506F  0243DCDF  830744CF  74000000  00000000
(    320)   44D1F480  0540C000  000040C0  00000040  72936A0A  3FFD94C6  094057A3  430C8F7E  EC969C44  41635309
```

2

14

I

I

I

010001001101100001

211 541_8 =

353

010000111001001010

207 112_8 =74

010001001101100110

211 546_8 =

358

```
  (   160)    43620000  0042EC00  00000000  00000042  C2E0720A  42E05B8D  02435F09  350A2CC3  4740042C  F5CCC703
  (   200)    40C00000  00304063  3C0F3FD3  EDC60E44  7022C70C  43438000  00000000  0000466E  E1120341  40000000
  (   240)    40C00000  004151B9  7A0A40D0  0E940C3F  F2D70409  3F7CE6AC  0142CA42  620F4279  74520E3F  C1340004
  (   280)    3ED623FA  033FE508  ED093EE3  9BE70641  60000000  00000000  00000000  00004140  00000035  FA778505
  (   320)    3E4821B5  023FD0C8  A10E3E77  C3000C3E  D9BF7202  3EF97A18  043EF13A  0EDC3EEC  2E6D003E  C2CCEC04
  (   360)    3E49BEE5  013E4BA1  47093DF4  70CA0401  30000301  00800003  00427000  000043CE  C0000043  C8000000
  (   400)    41D00000  00434C00  000042E4  00000040  C0000000  42E3FD86  0743527D  F50543C4  0E50CD27  D350070A
  (   440)    2948E606  0B000000  00002A7F  926B083F  CF36510A  44C01C8E  0543C650  00004CC0  00000043  D43FFB00
  (   480)    40C00000  0040C000  00004055  EA000F3F  F8389E0D  40721C42  003EDA08  C6004204  8EA30442  7C95F50E
  (   520)    3F7FE6C6  043E6833  D50B3D48  7D680840  7AE22E08  40C00000  00000000  00000000  00000040  C0000000
  (   560)    3D5C2D7E  083E7F72  4A0C3EF9  5C75023E  4EF6D901  3ED816D4  053F4F8C  27023F70  F364073F  4060FE00
  (   600)    3ECF113C  0F3E5868  2A0E3D76  C80A083D  D7673007  01800003  01008000  0003427C  00000043  C8000000

 EOJ    STOP REQUESTED IN FILE     1

 EOJ         DUMP STOPPED AFTER FILE   1          # OF PERMANENT READ ERRORS   0

START TIME 11/12/81  09:05:58         STOP TIME 11/12/81  09:06:17
```

$$